ORIGINAL PAPER

The numerical investigation of spreading process of two viscoelastic droplets impact problem by using an improved SPH scheme

Tao Jiang · Lin-Guang Lu · Wei-Gang Lu

Abstract In this paper, the spreading process of two XPP model droplets impacting on a plate in sequence at low Reynolds number is numerically simulated by using an improved smoothed particle hydrodynamics (I-SPH) method. The I-SPH method is a coupled approach which uses the traditional SPH (TSPH) method near the boundary domain and uses a kernel-gradient-corrected SPH method in the interior of fluid flow for the reason of remedying the accuracy and stability of TSPH. Meanwhile, an artificial stress term and a periodic density re-initialization technique are presented to eliminate the tensile instability and restrain pressure oscillation, respectively. A new boundary treatment is also adopted. The ability and merit of proposed I-SPH method combined with other techniques are first illustrated by simulating three typical examples. Subsequently, the deformation phenomena of two viscoelastic droplets impacting and spreading on a plate in sequence are numerically investigated. Particularly, the influences of the falling time interval, Weissenberg number and other rheological parameters on the deformation process are studied respectively. All numerical results agree well with the available data.

T. Jiang
Department of Mathematics, Yangzhou University,
Yangzhou 225002, China
e-mail: jtrjl_2007@126.com

T. Jiang
Coding and Cryptography Laboratory, Yangzhou University,
Yangzhou, China

L.-G. Lu (✉) · W.-G. Lu
College of Hydraulic Science & Engineering, Yangzhou University,
Yangzhou, China
e-mail: lglu@yzu.edu.cn

1 Introduction

In today's industry, the free surface flow of polymer melts plays an important role, for example the surface coating, extrusion, container filling in the pharmaceutical industries of polymer [1]. Almost all the non-Newtonian fluids exhibit some special non-linear behaviors, e.g. the viscoelastic or shear-thinning behavior, which have significant effects on the deformation process of polymer melt. In the deformation process, the impacting and spreading of liquid droplets on solid surfaces play a crucial role [2–4]. However, the numerical study of two viscoelastic droplets impacting and spreading on a plate has received little attention. In order to illustrate the viscoelastic behaviors and complex deformation process of two viscoelastic droplets impact, a suitable polymer model is needed. Here, the extended Pom–Pom (XPP) model [5], which describes branched polymer melts and the non-linear viscoelastic concentrated polymer materials, is studied. Moreover, the XPP model can degenerate to the Oldroyd-B model, which is often used to describe the viscoelastic polymer materials and is also considered in this work.

In the past few decades, many numerical methods have been proposed to solve the Navier–Stokes equations, such as the grid-based finite difference methods (FDM), finite volume method (FVM) and finite element methods (FEM) and so on. However, these mesh-based methods often encounter some numerical difficulties such as serious mesh distortion when they are used to simulate the large deformation or high gradient problems, and the mesh generation process is expensive. Moreover, the grid-based methods mentioned above

need an extra technique to capture the complex free surface, for example, marker and cell (MAC) [6], volume of fluid (VOF) [7] and level set [8,9]. Although they have been successfully applied to various free surface problems, there exist some defects in the techniques mentioned above.

For the reasons mentioned above, various mesh-free methods have been developed for the discontinuity or large deformation problems. Among these mesh-less methods [10–13], the smoothed particle hydrodynamics (SPH) method [11,13] is the earliest one and has been widely used which employs Lagrangian description of motion. SPH method has several advantages over the grid-based methods: (a) Complex free surfaces are modeled easily and naturally without the need of extra tracking technique; (b) It is easy to program for complex problems compared with grid-based methods. In 1994, SPH method was firstly used to deal with fluid dynamic problems [14,15]. From then, it has been applied to many areas such as viscous flows [16,17], incompressible fluids [18,19], multiphase flows [20–22], turbulence modeling [23], viscoelastic flows [24,25], and viscoelastic free surface flows [4,26].

Unfortunately, SPH method has two major drawbacks, that is, the low accuracy and numerical/tensile instability which must be remedied before it becomes a useful and robust tool. Therefore, some improved SPH methods based on Taylor series expansion have been proposed for different dynamic problems to restore the consistency [27–37] of the kernel and gradient particle approximations of the conventional SPH method, for instance, the corrected smoothed particle hydrodynamics method (CSPM) [30], finite particle method (FPM) [36], the modified SPH (MSPH) method [32,33] and the symmetric SPH (SSPH) method [34,35]which are mainly applied to elastic–dynamic problems in solid materials. Although the improved methods mentioned above have higher accuracy than traditional SPH method, some disadvantages still exist: the local matrix is asymmetric except for SSPH method, which can cause numerical instability; the choice of the kernel function is limited for solving the partial differential equations (PDEs) with higher derivatives; FPM/MSPH method is complicated to be extended to complex free surface flows problems, which can be seen from their construction process [32–36]. Moreover, the corrected kernel gradient scheme [30] has been introduced into the discretized schemes of TSPH and extensively applied to viscous fluid mechanic problems [38–40] in recent years. However, the corrected kernel gradient scheme mentioned above has not been extended to the viscoelastic free surface problems until now in our knowledge, and the involved local matrix is easily singular near the boundary region.

In this paper, a balanced improved SPH method is proposed and extended to simulate the free surface flows of polymer melts in this paper, which compromises the accuracy, the stability and computational efficiency of the traditional SPH,

MSPH (or SSPH) and the kernel-gradient-correction SPH (KGC-SPH). The proposed improved SPH method (I-SPH) is motivated by coupling the traditional SPH (TSPH) method with a KGC-SPH method, which possesses higher accuracy and better stability than SPH. The KGC-SPH method is only used in the inner region, and its construction process is based on the particles interaction and the concept of Taylor series to modify the TSPH, that is, directly correcting the kernel gradient of the discretized momentum equation, introducing the normal corrected kernel gradient scheme into the discretized schemes of viscous stress and elastic stress equations. Meanwhile, an artificial stress (AS) term is proposed and added into the discretized scheme of momentum equation to eliminate the tensile instability. A periodic density re-initialization (DR) method based on the corrected kernel estimate [32] of a Taylor series expansion is proposed to overcome the problem of the consistency among mass, density and the occupied area. Moreover, a new boundary condition is presented to treat the rigid plate, which is easier to implement than those in [4,26,40]. It is worth noting that the proposed modified SPH method has some merits and differences over than our previous publication works (e.g. [37,40]). The main merits or differences lie in: (1) a coupled particle method based on the corrected kernel gradient is first proposed and extended to simulate viscoelastic free surface flow based on the XPP model; (2) a new AS term is presented to eliminate the particle cluster phenomenon, which is more easily enforced than that in [26]. Indeed, the presented improved SPH schemes for viscoelastic constitutive model is derived from the extended application of the improved particle method for viscous fluid in [37,40], and the present coupled method compromises the advantages between the traditional SPH and the improved SPH method in [37,40].

In this work, the deformation process of two viscoelastic droplets impacting and spreading over a rigid plate in sequence is mainly investigated using the proposed I-SPH method combined with boundary treatment, and the influences of the falling time interval of two droplets and other model parameters (i.e. Weissenberg number) on the deformation process are discussed. The structure of this article is organized as follows: In Sect. 2, the governing equations for viscoelastic fluid flow are introduced; Sect. 3 describes the I-SPH discretized scheme of the Navier–Stokes equations based on the XPP model, including boundary conditions, artificial viscosity (AV) and AS; The validity and necessity of the AS and DR in the I-SPH method are tested in Sect. 4, and the merits of proposed I-SPH combined boundary condition treatment is also illustrated. Subsequently, the challenging example of single viscoelastic droplet impacting on a plate is simulated and compared with other results. In Sect. 5, the deformation process of two XPP droplets impacting on a plate with different time intervals are mainly numerical investigated using the proposed I-SPH, and the influences

of rheological parameters on the deformation are discussed; Conclusions and remarks are reported in Sect. 6.

2 Basic equations for the viscoelastic fluid

2.1 Governing equations

In a Lagrangian frame, the viscoelastic fluid flow is governed by the conservation of mass and momentum equations, together with a non-linear constitutive equation. The isothermal, compressible fluid is usually described by the following equations:

$$\frac{D\rho}{Dt} = -\rho \frac{\partial v^\beta}{\partial x^\beta}, \tag{1}$$

$$\frac{Dv^\alpha}{Dt} = \frac{1}{\rho} \frac{\partial \sigma^{\alpha\beta}}{\partial x^\beta} + g^\alpha, \tag{2}$$

where ρ denotes the fluid density, v^β the βth component of the fluid velocity, $\sigma^{\alpha\beta}$ the (α, β)th component of the total stress tensor, g^α the αth component of the gravitational acceleration and the $D/Dt = \partial/\partial t + v^\beta \cdot \left(\partial/\partial x^\beta\right)$ is the material derivative. The spatial coordinates x^β and time t are the independent variables.

The total stress tensor in Eq. (2) is commonly made up of the isotropic pressure p, the components of viscous stress $2\eta_s d^{\alpha\beta}$ and extra stress tensor $T^{\alpha\beta}$ (which is the polymer contribution stress or elastic stress of viscoelastic fluid, and that is measured by the following Eqs. (4)–(7) in this paper)

$$\sigma^{\alpha\beta} = -p\delta^{\alpha\beta} + 2\eta_s d^{\alpha\beta} + T^{\alpha\beta}, \tag{3}$$

here $\delta^{\alpha\beta} = 1$ if $\alpha = \beta$ and $\delta^{\alpha\beta} = 0$ if $\alpha \neq \beta$. $d^{\alpha\beta} = (1/2)\left(\left(\partial v^\alpha/\partial x^\beta\right) + \left(\partial v^\beta/\partial x^\alpha\right)\right)$ is the (α, β)th component rate of deformation tensor. The η_s is the Newtonian solvent contribution viscosity. In order to study a viscoelastic behavior of polymer material, the related constitutive equation will be given in the next subsection.

2.2 XPP model

In order to study the influence of viscoelastic behavior on free surface in polymer flow process, we employed the following extended pom–pom model (XPP) in multi-mode form [5,41,42] in the presented numerical simulations. The XPP model has two important features: (1) the dependence of melt rheology upon the polymer molecular structure; (2) the spectrum of relaxation time to be taken into account leads to two partial differential equations, one for orientation and one for stretch. The constitutive equation for the XPP model is

$$f(\lambda, \mathbf{T})\mathbf{T} + \lambda_{0b}\overset{\triangledown}{\mathbf{T}} + G_0\left[f(\lambda, \mathbf{T}) - 1\right]\mathbf{I}$$
$$+ \frac{\alpha_0}{G_0}\mathbf{T} \cdot \mathbf{T} = 2\lambda_{0b}G_0\mathbf{d}, \tag{4}$$

where $\mathbf{T}$ is the viscoelastic stress of polymeric contributions, and the function $f(\lambda, \mathbf{T})$ is given by

$$f(\lambda, \mathbf{T}) = \frac{2}{er}e^{\nu(\lambda-1)}\left(1 - \frac{1}{\lambda}\right) + \frac{1}{\lambda^2}\left(1 - \frac{\alpha_0 I_{\mathbf{T}\cdot\mathbf{T}}}{3G_0^2}\right), \tag{5}$$

and the symbol "$\overset{\triangledown}{\cdot}$" represents the following upper-convected derivative

$$\overset{\triangledown}{\mathbf{T}} = \frac{D\mathbf{T}}{Dt} - \mathbf{T} \cdot (\nabla\mathbf{u}) - (\nabla\mathbf{u})^{\mathrm{T}} \cdot \mathbf{T}, \tag{6}$$

$er = \lambda_{0s}/\lambda_{0b}$ (λ_{0b} and λ_{0s} are the orientation and backbone stretch relaxation time respectively), G_0 is the linear relaxation modulus, I refers to the trace of a tensor. The constitutive equation possesses the features of Giesekus model since a non-zero second normal stress difference is predicted when the anisotropy parameter $\alpha_0 \neq 0$. In the XPP model, the backbone stretch λ is related to the viscoelastic stress tensor

$$\lambda = \sqrt{1 + \frac{|I_{\mathbf{T}}|}{3G_0}}, \tag{7}$$

where the symbol "$|\cdot|$" represents the absolute value. The parameter ν in the exponential term in Eq. (5) is incorporated into the stretch relaxation time to remove the discontinuity from the gradient of the extensional viscosity. Its value is found to be inversely proportional to the number of arms q, $\nu = 2/q$.

Here, the following parameters are introduced, namely the total viscosity $\eta = \eta_s + \eta_p$, $\eta_p = G_0\lambda_{0b}$, $\varepsilon = \lambda_{0s}/\lambda_{0b}$, $\beta_0 = \eta_s/(\eta_s + G_0\lambda_{0b})$.

Specially, the Eq. (2) degenerates to the equation of motion for Oldroyd-B fluid when $\alpha_0 = 0$ and $f(\lambda, \mathbf{T}) = 1$ in Eq. (4). In addition, if $\beta_0 = 0$ then the UCM model is obtained. It should be noted that two type constitutive models, that is, the XPP model and Oldroyd-B model, are all considered for comparison in this paper.

2.3 Equation of state

The incompressible flows were sometimes treated as slightly compressible flows by adopting a suitable equation of state in many previous works (see Monaghan [14] and Morris et al. [16]). Here, the incompressible flows are also treated as weakly compressible flows using the following equation of state [25]

$$p(\rho) = c^2\rho^2/2\rho_0, \tag{8}$$

where c is the speed of sound and ρ_0 is reference density. An artificial, lower sound speed is usually used to avoid the instability and extremely small time steps. To keep the density variation of fluid less than 1% of the reference density, the Mach number M ($M \equiv V/c$, where V is a typical reference velocity) [12,13] must be smaller than 0.1. In other

words, the sound speed must be higher ten times than maximum fluid velocity.

3 Improved SPH scheme

In this section, an improved particle scheme is proposed for solving the governing equation based on the viscoelastic fluid model, which is motivated by improving the numerical accuracy and stability of TSPH scheme (see Sect. 3.1) and named the improved SPH (I-SPH) method (see Sect. 3.2). The I-SPH method couples TSPH method with KGC-SPH method, which possesses higher accuracy and better stability than TSPH. The KGC-SPH method is achieved by improving the TSPH with symmetric scheme, in which the construction process is based on the particles interaction and the concept of Taylor series, correcting the first order kernel gradient of SPH. The TSPH scheme and I-SPH scheme for the XPP fluid flow are described as follows.

3.1 Traditional SPH (TSPH) scheme

The TSPH method [12,13] is based on the interpolation theory, which is the theory of integral interpolates using a kernel function. In TSPH method, the fluid domain Ω is discretized into a finite number of particles, where all the relevant physical quantities are approximated in terms of the integral representation over neighboring particles. Each particle carries a mass m, velocity $\mathbf{v}$, and other physical quantities depending on the problem. Any function f and its first derivative defined at the position $\mathbf{x} = (x, y)$ can be usually expressed by the following integral (see [12]).

$$\langle f(\mathbf{x}) \rangle = \int_{\Omega} f(\mathbf{x}') W(\mathbf{x} - \mathbf{x}', h) d\mathbf{x}', \tag{9}$$

$$\langle \nabla f(\mathbf{x}) \rangle = \int_{\Omega} f(\mathbf{x}') \nabla W d\mathbf{x}' - f(\mathbf{x}) \int_{\Omega} \nabla W d\mathbf{x}', \tag{10}$$

where W represents the kernel function (or smoothing function) and h denotes the smoothing length defining the influence area of W. The kernel function W is usually required to meet three properties (see [12–16]), namely the positive property $W(\mathbf{x} - \mathbf{x}', h) \geq 0$, Dirac function property $\lim_{h \to 0} W(|\mathbf{x} - \mathbf{x}'|, h) = \delta(|\mathbf{x} - \mathbf{x}'|)$, normalization condition $\int_{\Omega} W(|\mathbf{x} - \mathbf{x}'|, h) d\mathbf{x}' = 1$, and the compact property $W(|\mathbf{x} - \mathbf{x}'|, h) > 0$ over Ω, $W(|\mathbf{x} - \mathbf{x}'|, h) = 0$ when $|\mathbf{x} - \mathbf{x}'| > \kappa h$ (where κ is a constant).

By applying integral principle by part and the divergence theorem to Eqs. (9) and (10), the particle discretized scheme of TSPH for a function $f(\mathbf{x})$ and its first derivative at the position $\mathbf{x} = (x, y)$ for particle i can be written in the condensed forms

$$f_i = \sum_j \frac{m_j}{\rho_j} f_j W_{ij}, \tag{11}$$

$$\left(\frac{\partial f}{\partial \mathbf{x}_i} \right) = \sum_j \frac{m_j}{\rho_j} (f_j - f_i) \frac{\partial W_{ij}}{\partial \mathbf{x}_i}, \tag{12}$$

where m_j and ρ_j are the mass and density of the jth particle, and $f_j = f(\mathbf{x}_j) . m_j/\rho_j$ represents the occupied volume by the jth particle. The $W_{ij} = W(|\mathbf{x}_i - \mathbf{x}_j|, h)$, $\partial W_{ij}/\partial \mathbf{x}_i = -\partial W_{ji}/\partial \mathbf{x}_j$.

The smoothing function W is related not only with the accuracy but also with the efficiency and stability of the resulting algorithm. As shown in [43], the Wendland function can produce more accurate results than the common spline kernel functions (e.g. the cubic or quintic splines function), which is also roughly illustrated in Sect. 4 (see Fig. 2). Therefore, the quintic Wendland kernel function is adopted in this work, which is

$$W_{ij} = W(r, h)$$
$$= w_0 \begin{cases} [2 - (r/h)]^4 [(2r/h) + 1], & 0 \leq r/h < 2 \\ 0, & r/h \geq 2, \end{cases} \tag{13}$$

where the $r = |\mathbf{x}_i - \mathbf{x}_j|$ and the normalization factor w_0 is $7/(64\pi h^2)$. Here, the smoothing length h is given by $1.0d_0 - 1.5d_0$, where d_0 is the initial distance between neighboring particles. The compact support domain size is $2h$.

Considering the discrete gradient Eq. (12) and the following identity: $\frac{1}{\rho} \frac{\partial \sigma^{\alpha\beta}}{\partial x^\beta} = \frac{\partial (\sigma^{\alpha\beta}/\rho)}{\partial x^\beta} + \frac{\sigma^{\alpha\beta}}{\rho^2} \frac{\partial \rho}{\partial x^\beta}$, the particle discretization schemes of the governing equations can be obtained at the particle i

$$\left(\frac{D\rho}{Dt} \right)_i = \rho_i \sum_j \frac{m_j}{\rho_j} (v_i^\beta - v_j^\beta) \frac{\partial W_{ij}}{\partial x_i^\beta}, \tag{14}$$

$$\left(\frac{Dv^\alpha}{Dt} \right)_i = \sum_j m_j \left(\frac{\sigma_i^{\alpha\beta}}{\rho_i^2} + \frac{\sigma_j^{\alpha\beta}}{\rho_j^2} \right) \frac{\partial W_{ij}}{\partial x_i^\beta} + g^\alpha, \tag{15}$$

where v^β is the βth component of the fluid velocity, $\sigma^{\alpha\beta}$ is the (α, β)th component of the total stress tensor and x^β is the component of spatial coordinate.

The particle discretization scheme of total stress Eq. (3) can be defined as

$$\sigma_i^{\alpha\beta} = -p\delta^{\alpha\beta} + \beta_0 \eta \left(\kappa_i^{\alpha\beta} + \kappa_i^{\beta\alpha} \right) + \left(T^{\alpha\beta} \right)_i, \tag{16}$$

where $\kappa_i^{\alpha\beta}$ denotes the following velocity gradient

$$\kappa_i^{\alpha\beta} = \left(\frac{\partial v^\alpha}{\partial x^\beta} \right)_i = \sum_j \frac{m_j}{\rho_j} (v_j^\alpha - v_i^\alpha) \frac{\partial W_{ij}}{\partial x_i^\beta}, \tag{17}$$

thus the discretized scheme of constitutive Eqs. (4) and (5) for the XPP model is given by

$$\left(\frac{DT^{\alpha\beta}}{dt}\right)_i = \kappa_i^{\alpha\gamma} T_i^{\gamma\beta} + \kappa_i^{\beta\gamma} T_i^{\gamma\alpha} - \frac{f(\lambda, T_i)}{\lambda_{0b}} T_i^{\alpha\beta}$$
$$- \frac{(1-\beta_0)\eta}{(\lambda_{0b})^2} \left[f(\lambda, T_i) - 1\right] \delta^{\alpha\beta}$$
$$- \frac{\alpha_0}{(1-\beta)\eta} T_i^{\alpha\gamma} T_i^{\gamma\beta} + \frac{(1-\beta_0)\eta}{\lambda_{0b}} \left(\kappa_i^{\alpha\beta} + \kappa_i^{\beta\alpha}\right),$$

$$(18)$$

where

$$f(\lambda, T_i) = \frac{2}{er} e^{v(\lambda-1)} \left(1 - \frac{1}{\lambda}\right)$$
$$+ \frac{1}{\lambda^2} \left(1 - \left(\frac{\lambda_{0b}}{3(1-\beta_0)\eta}\right)^2 \alpha_0 T_i^{\alpha\beta} T_i^{\alpha\beta}\right),$$

$$\lambda = \sqrt{1 + \frac{\lambda_{0b} |T_i^{\alpha\alpha}|}{3(1-\beta_0)\eta}},$$

$$(19)$$

3.2 I-SPH scheme

In order to restore the particle approximations consistency and improve the numerical accuracy and stability of TSPH method, the corrected symmetric kernel gradient scheme [40] and the Taylor expansion concept [30–33] are considered for the first-order derivative of Eqs. (14), (15) and (17), respectively. According to Ref. [40] and the Taylor expansion concept, the second order Taylor expansion of the first term in Eq. (10) can be obtained by

$$\int_{\Omega} f\left(\mathbf{x}'\right) \nabla W d\mathbf{x}' = f(\mathbf{x}) \int_{\Omega} \nabla W d\mathbf{x}'$$
$$+ \frac{\partial f(\mathbf{x})}{\partial x} \int_{\Omega} (x' - x) \nabla W d\mathbf{x}'$$
$$+ \frac{\partial f(\mathbf{x})}{\partial y} \int_{\Omega} (y' - y) \nabla W d\mathbf{x}' + O(h^2),$$

$$(20)$$

Substituting Eq. (20) into Eq. (10), we can get the following kernel approximation scheme

$$\langle \nabla f(\mathbf{x}) \rangle = \frac{\partial f(\mathbf{x})}{\partial x} \int_{\Omega} (x' - x) \nabla W d\mathbf{x}'$$
$$+ \frac{\partial f(\mathbf{x})}{\partial y} \int_{\Omega} (y' - y) \nabla W d\mathbf{x}' + O(h^2),$$

$$(21)$$

and particle approximation scheme

$$\langle \nabla f(\mathbf{x}_i) \rangle = \frac{\partial f(\mathbf{x}_i)}{\partial x_i} \sum_{j=1} \frac{m_j}{\rho_j} x_{ji} \nabla_i W_{ij} + \frac{\partial f(\mathbf{x}_i)}{\partial y_i} \sum_{j=1} \frac{m_j}{\rho_j} y_{ji} \nabla_i W_{ij},$$

$$(22)$$

where $x_{ji} = x_j - x_i$, $y_{ji} = y_j - y_i$.

Comparing Eq. (22) with Eq. (12), it leads to

$$\frac{\partial f(\mathbf{x}_i)}{\partial x_i} \sum_{j=1} \frac{m_j}{\rho_j} x_{ji} \frac{\partial W_{ij}}{\partial x_i} + \frac{\partial f(\mathbf{x}_i)}{\partial y_i} \sum_{j=1} \frac{m_j}{\rho_j} y_{ji} \frac{\partial W_{ij}}{\partial x_i}$$
$$= \sum_{j=1} \frac{m_j}{\rho_j} (f_j - f_i) \frac{\partial W_{ij}}{\partial x_i},$$

$$(23)$$

$$\frac{\partial f(\mathbf{x}_i)}{\partial x_i} \sum_{j=1} \frac{m_j}{\rho_j} x_{ji} \frac{\partial W_{ij}}{\partial y_i} + \frac{\partial f(\mathbf{x}_i)}{\partial y_i} \sum_{j=1} \frac{m_j}{\rho_j} y_{ji} \frac{\partial W_{ij}}{\partial y_i}$$
$$= \sum_{j=1} \frac{m_j}{\rho_j} (f_j - f_i) \frac{\partial W_{ij}}{\partial y_i},$$

$$(24)$$

This system can be rewritten in the form of matrix equation as

$$A \begin{pmatrix} \frac{\partial f(\mathbf{x}_i)}{\partial x_i} \\ \frac{\partial f(\mathbf{x}_i)}{\partial y_i} \end{pmatrix} = \begin{pmatrix} \sum_{j=1} \frac{m_j}{\rho_j} (f_j - f_i) \frac{\partial W_{ij}}{\partial x_i} \\ \sum_{j=1} \frac{m_j}{\rho_j} (f_j - f_i) \frac{\partial W_{ij}}{\partial y_i} \end{pmatrix},$$

$$(25)$$

where $A = \sum_{j=1} \frac{m_j}{\rho_j} \begin{pmatrix} x_{ji} \frac{\partial W_{ij}}{\partial x_i} & y_{ji} \frac{\partial W_{ij}}{\partial x_i} \\ x_{ji} \frac{\partial W_{ij}}{\partial y_i} & y_{ji} \frac{\partial W_{ij}}{\partial y_i} \end{pmatrix}.$

Adopting the idea in [34,35], we use "$(x_j^\alpha - x_i^\alpha) W_{ij}$" instead of "$\partial W_{ij}/\partial x_i^\alpha$" in Eq. (25), and Eq. (25) becomes

$$\begin{pmatrix} \frac{\partial f(\mathbf{x}_i)}{\partial x_i} \\ \frac{\partial f(\mathbf{x}_i)}{\partial y_i} \end{pmatrix} = \sum_{j=1} \frac{m_j}{\rho_j} (f_j - f_i) \begin{pmatrix} \partial \tilde{W}_{ij}^{CS}/\partial x_i \\ \partial \tilde{W}_{ij}^{CS}/\partial y_i \end{pmatrix},$$

$$(26)$$

where

$$\begin{pmatrix} \partial \tilde{W}_{ij}^{CS}/\partial x_i \\ \partial \tilde{W}_{ij}^{CS}/\partial y_i \end{pmatrix} = (A^s)^{-1} \begin{pmatrix} (x_j - x_i) W_{ij} \\ (y_j - y_i) W_{ij} \end{pmatrix},$$

$$A^s = \begin{pmatrix} \sum_{j=1}^N \frac{m_j}{\rho_j} x_{ji} x_{ji} W_{ij} & \sum_{j=1}^N \frac{m_j}{\rho_j} y_{ji} x_{ji} W_{ij} \\ \sum_{j=1}^N \frac{m_j}{\rho_j} x_{ji} y_{ji} W_{ij} & \sum_{j=1}^N \frac{m_j}{\rho_j} y_{ji} y_{ji} W_{ij} \end{pmatrix}. \quad (27)$$

Note that the kernel gradient correction procedure mentioned above is different from that in [30], and its (i.e. Eq. (27)) advantages have been discussed in [35,37,40].

Applying the corrected kernel gradient scheme (27) to the discretized schemes (14), (15) and (17), we can get the following KGC-SPH scheme for the viscoelastic fluid flow based on the XPP model.

$$\left(\frac{D\rho}{Dt}\right)_i = \rho_i \sum_j \frac{m_j}{\rho_j} (v_i^\beta - v_j^\beta) \frac{\partial \tilde{W}_{ij}^{CS}}{\partial x_i^\beta},$$

$$(28)$$

$$\left(\frac{Dv^\alpha}{Dt}\right)_i = \sum_j m_j \left(\frac{\sigma_i^{\alpha\beta}}{\rho_i^2} + \frac{\sigma_j^{\alpha\beta}}{\rho_j^2}\right) \frac{\partial \tilde{W}^{CS}}{\partial x_i^\beta} + g^\alpha,$$

$$(29)$$

$$\kappa_i^{\alpha\beta} = \left(\frac{\partial v^\alpha}{\partial x^\beta}\right)_i = \sum_j \frac{m_j}{\rho_j} (v_j^\alpha - v_i^\alpha) \frac{\partial \tilde{W}_{ij}^{CS}}{\partial x_i^\beta}$$

$$(30)$$

It should be noted that the corrected scheme (29) mentioned above is different from those in [38–40]. The corrected scheme Eq. (29) of momentum equation restores the feature of particles interaction in the KGC-SPH method, which can reduce the serious defect of particles cluster (or tensile instability) when the viscoelastic droplet impacting on plate. Moreover, the correction of KGC-SPH method without kernel derivative (see (27)) has some merits of SSPH method (see [34,35]).

The I-SPH method is motivated by improving the numerical accuracy and stability of TSPH scheme, which is based on the idea of coupling TSPH method with the KGC-SPH method. We use TSPH near the free surface (or boundary particles) and use the KGC-SPH in the interior fluid field, and the boundary particles or free surface particles may be identified by particle densities (see [44]).

The coupled I-SPH approximate schemes of the XPP model are obtained by using Eqs. (14)–(17) for the boundary particles and using Eqs. (28)–(30) for the interior particles, that is

$$\left(\frac{\mathrm{D}\rho}{\mathrm{D}t}\right)_i = \rho_i \sum_j \frac{m_j}{\rho_j}(v_i^\beta - v_j^\beta)H_{ij}^\beta, \tag{31}$$

$$\left(\frac{\mathrm{D}u^\alpha}{\mathrm{D}t}\right)_i = \sum_j m_j \left(\frac{\sigma_i^{\alpha\beta}}{\rho_i^2} + \frac{\sigma_j^{\alpha\beta}}{\rho_j^2}\right)H_{ij}^\beta + g^\alpha. \tag{32}$$

$$\kappa_i^{\alpha\beta} = \left(\frac{\partial v^\alpha}{\partial x^\beta}\right)_i = \sum_j \frac{m_j}{\rho_j}(v_j^\alpha - v_i^\alpha)H_{ij}^\beta \tag{33}$$

where

$$H_{ij}^\beta = \begin{cases} \left(\partial W_{ij}/\partial x_i^\beta\right), & i \in \text{boundary particles} \\ \left(\partial \tilde{W}_{ij}^{CS}/\partial x_i^\beta\right), & i \in \text{interior particles} \end{cases} \tag{34}$$

At the end of each time-step, the position of each particle is updated using

$$\frac{\mathrm{D}x_i^\alpha}{\mathrm{D}t} = v_i^\alpha \tag{35}$$

3.3 Density re-initialization (DR) technique

In the SPH method, each particle has a fixed mass. If the number of particles is constant, mass conservation is intrinsically satisfied. However, the consistency between mass, density and the occupied area could not be enforced exactly (see [16]) if the evolved particle density is determinated by the evolution Eq. (1) for simulating the weakly compressible flows.

In order to overcome this problem, we use a second-order accuracy particle approximation scheme based on Taylor series expansion (see [32–34,44]) to periodically re-initialize the density field. According to the Taylor series expansion idea in [37,40], the function value and its first derivatives at

the particle i can be calculated as

$$f_i = \sum_j \frac{m_j}{\rho_j} f_j \tilde{W}_{ij} \tag{36}$$

$$\begin{cases} \left(\frac{\partial f}{\partial x}\right)_i = \sum_j \frac{m_j}{\rho_j} f_j \left(\frac{\partial \tilde{W}_{ij}}{\partial x_i}\right) \\ \left(\frac{\partial f}{\partial y}\right)_i = \sum_j \frac{m_j}{\rho_j} f_j \left(\frac{\partial \tilde{W}_{ij}}{\partial y_i}\right) \end{cases} \tag{37}$$

where the corrected kernel $\tilde{W}_{ij}$ and its derivative $\frac{\partial \tilde{W}_{ij}}{\partial x_i}, \frac{\partial \tilde{W}_{ij}}{\partial y_i}$ are given by

$$\left(\tilde{W}_{ij}, \frac{\partial \tilde{W}_{ij}}{\partial x_i}, \frac{\partial \tilde{W}_{ij}}{\partial y_i}\right)^T = \left(\sum_j \mathrm{A}(\mathbf{x}_i) V_j\right)^{-1} \times \left(W_{ij}, \frac{\partial W_{ij}}{\partial x_i}, \frac{\partial W_{ij}}{\partial y_i}\right)^T, \tag{38}$$

and the local coefficient matrix is

$$\mathrm{A}(\mathbf{x}_i) = \begin{pmatrix} W_{ij} & x_{ji} \cdot W_{ij} & y_{ji} \cdot W_{ij} \\ \frac{\partial W_{ij}}{\partial x_i} & x_{ji} \cdot \frac{\partial W_{ij}}{\partial x_i} & y_{ji} \cdot \frac{\partial W_{ij}}{\partial x_i} \\ \frac{\partial W_{ij}}{\partial y_i} & x_{ji} \cdot \frac{\partial W_{ij}}{\partial y_i} & y_{ji} \cdot \frac{\partial W_{ij}}{\partial y_i} \end{pmatrix}. \tag{39}$$

In this work, the idea of calculating the function value mentioned above is extended to re-initialize the density field, and let $f_j = \rho_j$ in Eq. (36).

$$\rho_i = \sum_j m_j W_{ij}^{Tay}, \tag{40}$$

where the corrected kernel function W_{ij}^{Tay} is given by

$$W_{ij}^{Tay} = \mathrm{B}\left[\sum_j \mathrm{A}(\mathbf{r}_i) V_j\right]^{-1} \mathrm{W}, \tag{41}$$

$$\mathrm{B} = (1, 0, 0), \qquad \mathrm{W} = \begin{pmatrix} W_{ij} \\ \partial W_{ij}/\partial x_i \\ \partial W_{ij}/\partial y_i \end{pmatrix} \tag{42}$$

Here $x_{ji} = x_j - x_i$, $y_{ji} = y_j - y_i$, and V_j is replaced by m_j/ρ_j. The particle approximations scheme Eqs. (40)–(42) possess C^0, C^1 consistency for boundary regions or irregularly distributed particles (see [32]).

When the DR method is applied in above SPH or I-SPH method, an 3×3 invertible matrix should be solved for each fluid particle, thus, the computing time is increased slightly. Considering the computational cost and the efficiency of using periodic DR, we can apply this procedure every fixed (about 20–50, see Sect. 4.2) time steps in our numerical simulations. Specially, to keep that the corrected particle approximations Eq. (40) at least have C^0 consistency on the whole domain, the matrix $\sum_j \mathrm{A}(\mathbf{r}_i) V_j$ may be replaced by $\sum_j W_{ij} V_j$ if the matrix in Eq. (41) is singular (it occurs occasionally).

3.4 Artificial viscosity (AV) model

According to previous works [16,45], an artificial viscosity term is usually adopted to increase the stability of TSPH method. The AV is first introduced to enhance the numerical stability and accuracy in the simulations of strong shock problems [45]. On the other hand, the AV term guarantees the conservation of angular momentum without external force when it is added into the momentum equation of TSPH schemes. For this reason, the AV term is usually also considered and employed in the SPH simulations of viscous or viscoelastic fluid flows problems with large deformation, which can be found in recent works [4,26]. Through the simulations of viscoelastic droplet impact problem in [4,26] and our numerical simulation experience of using TSPH or improved SPH method, we find that it is necessary to employ an AV term in the discrete momentum equation Eq. (30) for improving the numerical stability (see Sect. 4.2).

In this work, the following AV term (see [11,12]) is chosen and added into the discrete momentum equation Eq. (30) of I-SPH method, which is

$$\Pi_{ij} = \begin{cases} \dfrac{-\alpha_\Pi \bar{c}_{ij}\phi_{ij} + \beta_\Pi \phi_{ij}^2}{\bar{\rho}_{ij}}, & \mathbf{v}_{ij} \cdot \mathbf{r}_{ij} < 0 \\ 0, & \mathbf{v}_{ij} \cdot \mathbf{r}_{ij} \geq 0 \end{cases} \quad (43)$$

where

$$\phi_{ij} = \frac{h\mathbf{u}_{ij} \cdot \mathbf{r}_{ij}}{\left|\mathbf{r}_{ij}\right|^2 + 0.01h^2}, \quad \bar{c}_{ij} = \frac{c_i + c_j}{2}, \quad \bar{\rho}_{ij} = \frac{\rho_i + \rho_j}{2},$$

and $\mathbf{v}_{ij} = \mathbf{v}_i - \mathbf{v}_j$, $\mathbf{r}_{ij} = \mathbf{r}_i - \mathbf{r}_j$. $\quad (44)$

The $0.01h^2$ term is used to prevent numerical divergence when two particles get too close to each other. The α_Π and β_Π are usually chosen approximately equal to 1. In the AV, the first term associated with α_Π involves shear and bulk viscosity, while the second term associated with β_Π is similar to the von-Neumann–Richtmeyer viscosity for resolving shocks and is very important in preventing unrealistic particle penetration, especially for particles that are approaching each other at high speed. It is noting that the AV term mentioned above bears no relation to real fluid viscosity (see [45]).

3.5 Artificial stress (AS) model

In 1995, the "tensile instability" was first investigated in details by Swegle et al. [46], who pointed that the phenomenon of unphysical clustering of particles arises when the standard SPH method is applied to Euler problem. At present, a number of methods have been proposed to remove the tensile instability in elastic dynamics of solid materials. The artificial stress method [47,48] is one of the most successful approaches, which is successfully extended and applied to non-Newtonian fluid free surface flows [4,26]. In [47,48], it is considered that "tensile instability" is mainly caused by

tension (positive stress in tension), so that the adopted AS term [4,26] is only related to the positive stress. As pointed out in [46], the "tensile instability" is related to the sign of both the stress and the second derivative of the kernel function, which implies that the instability is not only caused by the tension but also the compression (negative stress in compression). Therefore, we extend the conclusions in [46–48] and use the following AS term to eliminate the "tensile instability" (or "particles cluster phenomenon")

$$f_{ij}^n \left(S_i^{\alpha\beta} + S_j^{\alpha\beta} \right), \quad (45)$$

where $f_{ij} = W_{ij}\left(\left|\mathbf{r}_i - \mathbf{r}_j\right|, h\right)/W_{ij}\left(d_0, h\right)$, n is an exponential factor and is often chosen to be 4 so that the repulsive force increases as $r(h \leq r \leq 2h)$ decreases from d_0 to zero. The components of the AS tensor $S_i^{\alpha\beta}$ is given as

$$S_i^{\alpha\beta} = \begin{cases} -b\sigma_i^{\alpha\beta}/\rho^2, & if \left(\sum_j W_{ij}^{''\alpha\beta}\right) \cdot \sigma_i^{\alpha\beta} > 0 \\ 0, & other \end{cases}, \quad (46)$$

where b is a positive parameter $(0 < b < 1)$, and the $W_{ij}^{''\alpha\beta} = \partial^2 W_{ij}/\left(\partial x^\alpha \cdot \partial x^\beta\right)$.

Indeed, the key aim of the AS term mentioned above is to introduce a repulsive force to prevent two neighboring fluid particles from getting too close when the two particles are in a state of tensile or compressible force, and subject to an attraction when two neighboring particles far from each. Moreover, the form of proposed AS term is simpler than the artificial stress form in [26], and it is more easily extended and applied to 3D problem.

Introducing the $K_{ij} = f_{ij}^n \left(S_i^{\alpha\beta} + S_j^{\alpha\beta} \right)$, the AV term Eq. (43) and the AS term Eq. (45) are added to the discretized momentum equation (32) of I-SPH, it leads to

$$\left(\frac{Dv^\alpha}{Dt}\right)_i = \sum_j m_j \left(\frac{\sigma_i^{\alpha\beta}}{\rho_i^2} + \frac{\sigma_j^{\alpha\beta}}{\rho_j^2} - \Pi_{ij}\delta^{\alpha\beta} + K_{ij} \right) H_{ij}^\beta + g^\alpha. \quad (47)$$

Compared our previous researches (e.g. [4,37,40]) with the proposed coupled method combined with other techniques, the main merit is that the present method compromises the advantages between the traditional SPH and other improved SPH method including our previous works and is more easily extended to applied than other improved SPH methods by observing their construction process (see [37]). Moreover, the I-SPH method combined with a new AS term and a DR technique is first proposed and extended to viscoealstic free surface flows based on the XPP model in this paper.

3.6 Time integration scheme

Here, we choose the predictor–corrector scheme to solve the system of ordinary differential equations (18), (31), (35)

and (47) due to that the predictor–corrector scheme possesses second-order accuracy and better stability. The predictor step consists of an Eulerian explicit evaluation of all quantities for each particle

$$\tilde{K}_i^{n+1} = K_i^n + \frac{\Delta t}{2} \Gamma_i^n, \tag{48}$$

where K_i represents the vector of the unknown variables $\left(\rho_i, v_i^\alpha, T_i^\alpha, x_i^\alpha\right)$ and Γ_i denotes the vector of right-hand sides of Eqs. (18), (31), (35) and (47). In the corrected step, the updated value of K_i at the end of each time step is given by

$$K_i^{n+1} = K_i^n + \frac{\Delta t}{2} \left(\Gamma_i^n + \tilde{\Gamma}_i^{n+1} \right), \tag{49}$$

As is well known, the time step and space step must satisfy the well-known Courant–Friedrichs–Lewy (CFL) condition for the purpose of ensuring the numerical stability. According to [44], we may choose the following stability condition

$$\Delta t \le \min \left[0.25 \frac{h}{c}, 0.125 \frac{h^2}{\upsilon_0} \right], \tag{50}$$

where $\upsilon_0 = \eta / \rho_0$ is the kinematic viscosity.

3.7 Boundary condition treatment

In most engineering problems, the physical boundary might be the surface of rigid bodies enclosing fluid or enclosed by fluid, fully or partially. The boundary can be stationary or in motion. The treatment of boundary conditions in SPH method has an important effect on the numerical results.

Several methods for treating rigid wall boundary conditions have been presented in previous work. There are mainly two methods, i.e. (1) the solid walls may be simulated by particles, which enforces repulsive force by employing an artificial repulsive force (see [12]) on inner fluid particles to prevent them from penetrating the wall. (2) The wall boundary conditions can also be modeled either by fixed particles [13] or by virtual particles that mirror the physical properties of inner fluid particles. The above methods of boundary treatment have been discussed in 2009 [49], and the literature shows that the virtual particles approach have better stability and affectivity than the artificial repulsive force method. So the boundary particles in this work do not employ an artificial repulsive force instead of adopting the virtual particles on approaching real particles to prevent fluid particles from penetrating rigid wall.

As shown in Fig. 1, the virtual particles are used to implement the boundary conditions on a rigid wall, which are located right on the rigid wall, namely "rigid particles". The rigid particles have fixed density and positions with at least a range of depth comparable with the compact support of the kernel used in the computations. In this paper, the initial distance between neighboring rigid particles is set to $d_0/2$ along the x-axis and equal to d_0 along the y-axis (d_0 as the initial
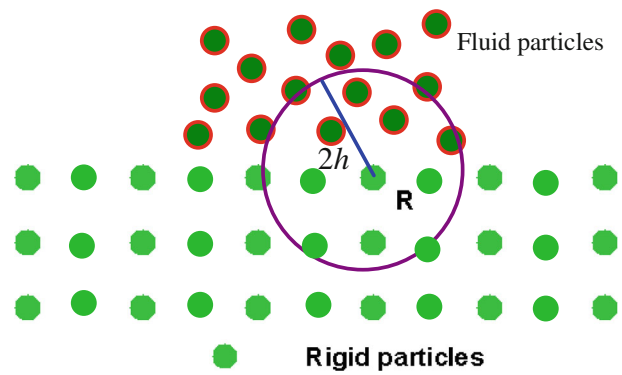

Fig. 1 The sketch of rigid particles

distance between neighboring fluid particles) for the better of preventing fluid particles from penetrating rigid wall.

The density of wall particles is not evolved and the non-slip condition is enforced on the solid wall and the positions of rigid particles remain fixed in time. The pressure and elastic stress on the wall particles are calculated according to the following approximation formulation

$$L_i = \sum_j L_j \left(2h - r_{ij} \right) / \sum_j \left(2h - r_{ij} \right). \tag{51}$$

where i represents the index of a wall particles and j denotes the index of its neighboring fluid particles only. The L_i represents the vector of variables $\left(p, T^{\alpha\beta} \right)_i$.

The boundary treatment mentioned above is feasible to prevent fluid particles from penetrating rigid wall (see Sect. 4) and possesses higher computational efficiency than that of proposed boundary treatment in [4,26], thus it is valid and easier to be implemented than those in [4,26].

Moreover, the following total stress-free condition must be satisfied in the computational domain for surface particles

$$\boldsymbol{\sigma} \cdot \mathbf{n} = 0, \tag{52}$$

where $\mathbf{n}$ denotes a unit normal vector to the surface. In this paper, the surface tensor is neglected and a Dirichlet boundary condition of zero pressure is given to the surface particles. This condition, i.e. Eq. (52), is satisfied naturally by the I-SPH method.

4 Numerical tests

In this section, some benchmark examples will be solved and compared with other numerical results to verify the accuracy of proposed I-SPH approach combined with the boundary condition treatment to simulate the viscoelastic fluid flow. Meanwhile, the validities of AV, AS and DR technique are also illustrated by simulating a single droplet impacting on plate based on the Oldryod-B fluid. Noting that the Oldroyd-B fluid model is considered in this section,

Fig. 2 Particle distributions obtained using different techniques: **a** TSPH with cubic spline kernel; **b** TSPH with quintic Wendland kernel; **c** I-SPH with quintic Wendland kernel and artificial stress (I-SPH-AS). ($Re = 100, t = 0.2$ s)
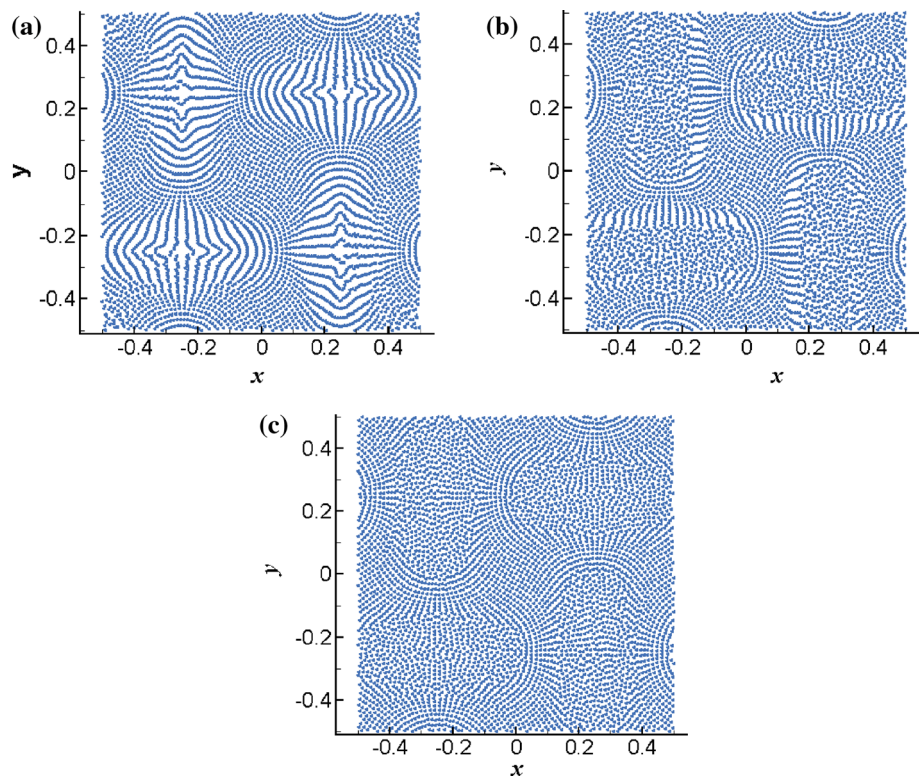
which can be obtained from the XPP constitutive model with $\alpha_0 = 0$, $f(\lambda, \tau) = 1$ in Eq. (5).

### 4.1 The accuracy of the I-SPH method

Example 1: Taylor–Green flow

In this subsection, the 2-D Taylor–Green flow (see [50]) of Newtonian fluid is first simulated to investigate the accuracy of the I-SPH method and the merit of the quintic Wendland kernel function. The Taylor–Green flow is a periodic array of decaying vortices in the plane, and its velocity components are given

$$u = -U e^{bt} \cos(2\pi x) \sin(2\pi y),$$
$$v = U e^{bt} \sin(2\pi x) \cos(2\pi y). \tag{53}$$

where $U = 1$m/s is the velocity scale, the computational periodic domain is performed on $[0, L] \times [0, L]$ with $L = 1$ m, the kinematic viscosity $\upsilon_0 = 0.01$ m^2/s and corresponding to the Reynolds number $Re = UL/\upsilon_0 = 100$; $b = -8\pi^2/Re$ is the decay rate of the velocity field.

Figure 2 shows the comparisons of particle distributions obtained using different numerical methods for the Taylor–Green flow. It can be observed that the TSPH results possess more obvious instability than the other numerical results. Meanwhile, we can know that the quintic Wendland kernel function has better stability than the conventional cubic spline kernel from Fig. 2a, b. The particle distributions obtained by
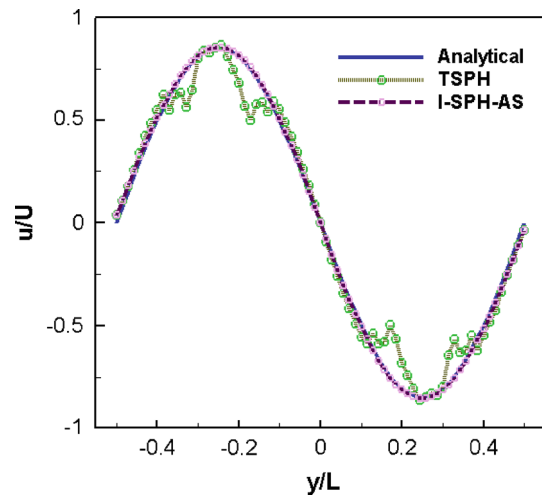
Fig. 3 The velocity profiles obtained using different methods at $x/L = 0.0$ m. ($Re = 100, t = 0.2$ s)

I-SPH method combined the artificial stress (I-SPH-AS) are more uniform than those obtained by the TSPH method due to the effect of AS technique combining with the corrected symmetric kernel gradient scheme and the quintic Wendland kernel function. Moreover, the tensile instability is well eliminated by the I-SPH method for simulating fluid flow which can be found from Fig. 2c. The effect of AS will be discussed in Sect. 4.2.

Figure 3 shows the velocity profiles at $x/L = 0.0$ obtained using different numerical methods with $Re = 100$, $t = 0.2$ s
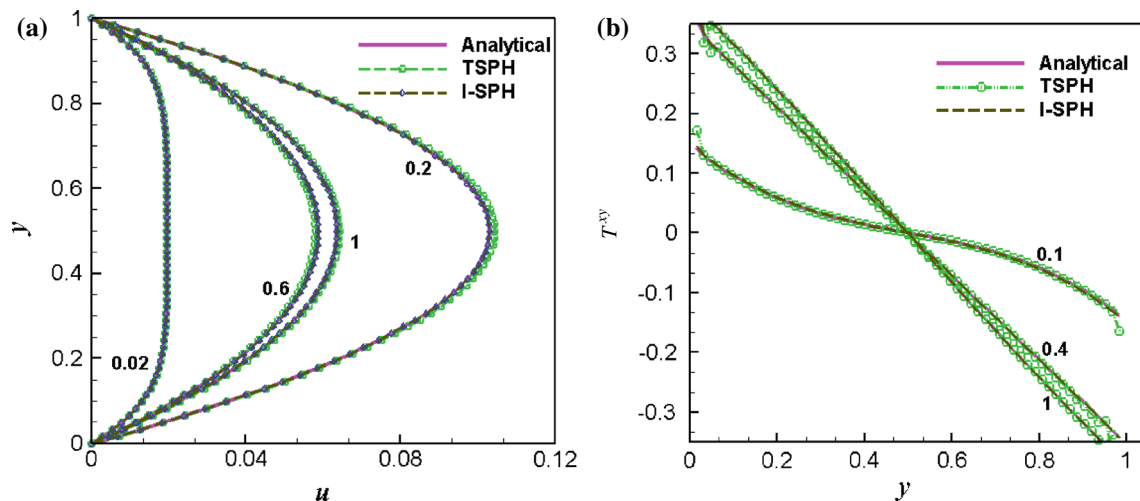
Fig. 4 Comparisons of different numerical results for the Oldroyd-B fluid flow $Re \approx 0.03$: **a** $u(y)$; **b** $T^{xy}(y)$

The I-SPH results of velocity component $u(y)$ are much closer to the analytical solutions than the other results, and the TSPH results appear small oscillations in Fig. 3. On the other hand, we can get that the proposed I-SPH combined with the AS term has higher accuracy and better stability than the TSPH method.

Example 2: Poiseuille flow

In order to further demonstrate the capacity of the proposed I-SPH method for solving viscoelstic fluid flow, Fig. 4 show the comparisons of the numerical results obtained using different numerical methods for the Poiseuille flow based on the Oldroyd-B fluid with different physical parameters. The planar flow involves flow between two stationary parallel, the infinite plates located at $y = 0$ and $y = L_0$. The Poiseuille flow describes that the initially stationary fluid is driven by a body force F paralleling to the x-axis and then removes. The analytical solutions of Poiseuille for the Oldroyd-B fluid have been given in [3,12].

In this simulation, all the non-dimensional physical quantities are set as: the characteristic velocity $U = FL_0^2/8\upsilon_0$, and corresponding to the Reynolds number $Re = UL_0/\upsilon_0$, the Weissenberg number $We = (\lambda_{ob}U)/L_0$; the ratio of viscosity $\beta_0 = 0.3$, the number of fluid particles is 31×61 and the other parameters values are: $L_0 = 1$, $\rho_0 = 1$, the sound speed $c = 10U_{max}$, the smoothing length $h = 1.1d_0$, the time step $dt = 10^{-4}$. Moreover, the kinematic viscosity $\upsilon_0 = 2$, the body force $F = 1$ corresponding to the $Re \approx 0.03$, the relaxation time $\lambda_{ob} = 0.2$ corresponding to the $We = 0.012$ in Fig. 4. The techniques of DR, AV and AS are all not adopted for the I-SPH method in this subsection.

From Fig. 4, it can be found that the I-SPH results are much closer to the analytical solutions than the TSPH results. It is worth noting that the shear elastic stress obtained using TSPH method has small oscillation near the boundary, which will

lead to instability versus time. Meanwhile, the overshooting phenomenon appears for Oldroyd-B fluid. Seeing Fig. 4, the advantages of the proposed I-SPH method over the TSPH method can be obtained as: (1) the I-SPH has higher accuracy than the TSPH for simulating the viscoelastic fluid flow; (2) the I-SPH method for capturing the overshooting phenomenon of velocity is more accurate than the TSPH method.

4.2 The validity of some techniques

In this subsection, the validity and necessity of DR, AV and AS introducing in the I-SPH method are discussed.

Example 1: Stretching of a Newtonian fluid droplet [44]

All the physical quantities are the same as those in [44], the reference density $\rho_0 = 1,000$ kg m^{-3}, the viscosity $\eta = 0.001$ kg m^{-1}s^{-1}, and the speed of sound $c = 1,400$ ms^{-1}. The initial geometry of the water drop is a circle of radius $R = 1$ m with its center located at the origin $(x = 0, y = 0)$. There is no external forces but a initial velocity field $v_0^x = -A_0x$, $v_0^y = A_0y$ with $A_0 = 100$ s^{-1} and the initial pressure field $p_0 = (1/2) \rho_0 A_0^2 [R^2 - (x^2 + y^2)]$. The number of fluid particles is 1961, and the time step $dt = 10^{-5}$ s. During the stretching process of water dropwhich should remain elliptical shape and the value of semi-minor axis times semi-major axis should remain constant. We let "M" denote the interval time step of the periodic DR of TSPH-DR, and the TSPH-DR method becomes the TSPH method if M = ∞.

Figure 5 shows the numerical results of the semi-minor axis obtained using TSPH-DR method with different M. We can see that the better results belong to M = 10 and 20. In fact, the more uniformly distributed the particles are, the better the numerical accuracy is. The accuracy of numerical results using TSPH can be improved by periodic DR with appropriate "M". In a word, the effect of the DR method
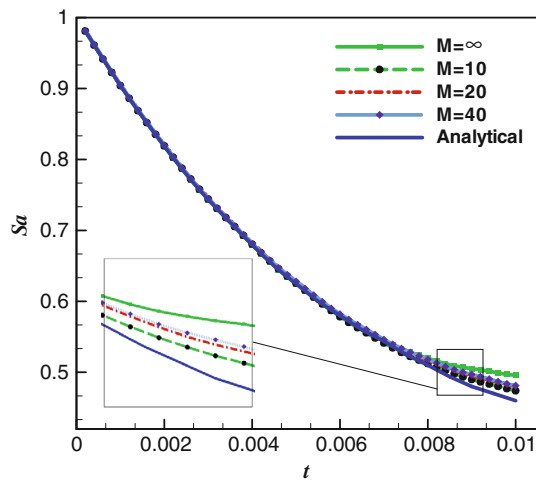
Fig. 5 Comparisons of numerical results obtained using TSPH-DR method about the semi-minor axis varying with time

used in the TSPH method is obvious. Observing the results of Fig. 5 and considering the computational cost and the effect of TSPH-DR with different "M", we choose the interval time step M = 25 in all the following numerical simulations.

Example 2: Evolution of a square Newtonian fluid patch [44]

The deformation process of rotation of a free surface square fluid patch is numerically illustrated to test the advantages of the AV and AS. The initial rotation velocity $v_0^x = \omega y$, $v_0^y = -\omega x$ ($\omega = 100$ denotes an arbitrary angular velocity), the initial pressure field $P_0 = 0$, and the other parameters are the same as in Fig. 5. The number of fluid particles is 51×51, and the time step $dt = 5 \times 10^{-6}$ s.

The shape of a square fluid patch obtained using different numerical methods are illustrated in Fig. 6 at $t = 0.016$ s. The parameters of AV and AS are $\alpha_{II} = 0.1$, $\beta_{II} = 0.2$, $b = 0.1$. Comparing with the Fig. 6a–d, we can know that the
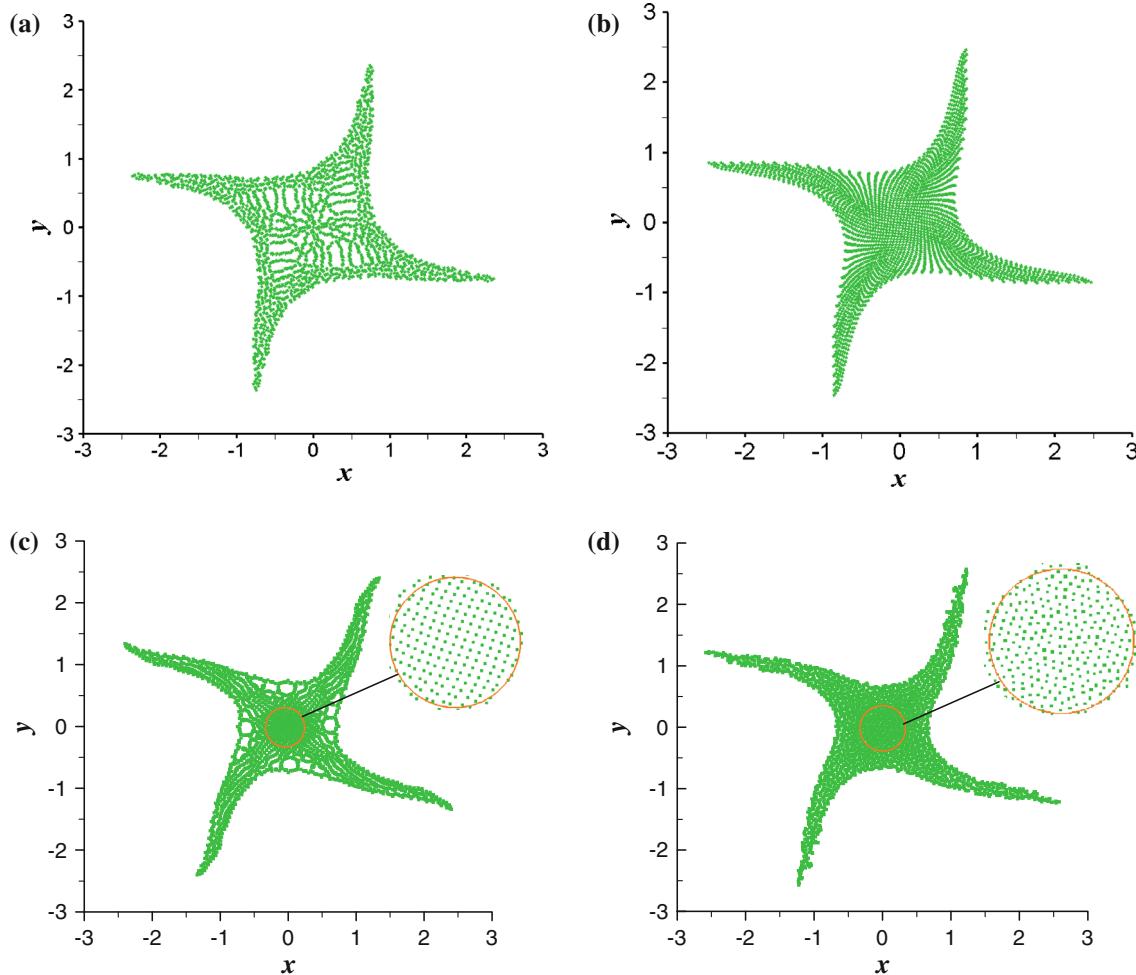
Fig. 6 The deformation process of a square fluid patch obtained by different methods at $t = 0.016$ s: **a** TSPH; **b** I-SPH-AV; **c** TSPH-AV; **d** TSPH-AS

(a) I-SPH

(b) I-SPH –AV

(c) I-SPH -AS

(d) I-SPH -AV-AS
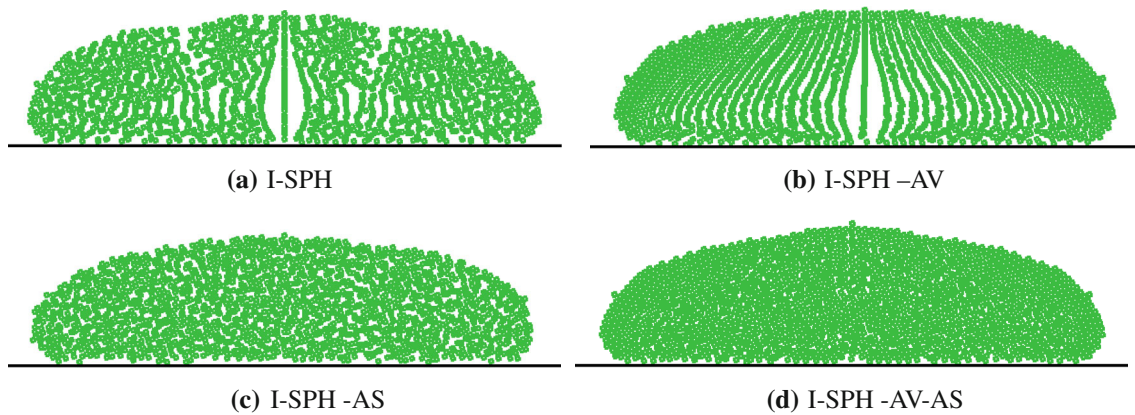
Fig. 7 The particles distributions of an Oldroyd-B drop impacting on plate obtained by different methods at dimensionless time $t \approx 2.1$

(a) I-SPH-AV-AS

(b) I-SPH-AV-AS-DI
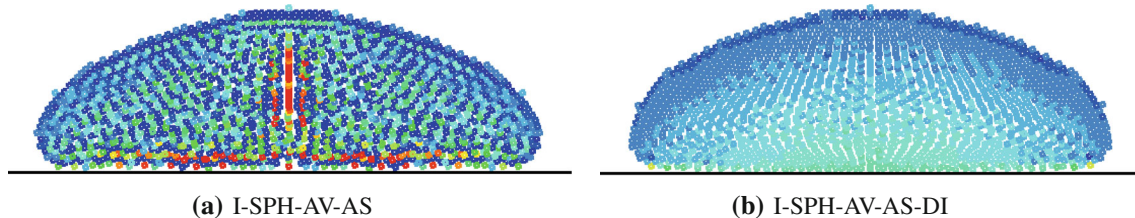
Fig. 8 The pressure distribution of an Oldroyd-B drop impacting on plate at dimensionless time $t \approx 1.8$

non-physical phenomenon of particles location for the TSPH method is improved by TSPH-AV, TSPH-AS and I-SPH-AV methods. Although the instability is improved by the AV and AS models, respectively (see Fig. 6c, d), the particles distribution is not uniform for the TSPH-AS results (see Fig. 6d) due to the influence of AS, which can reduce the numerical accuracy. The I-SPH-AV results are the best among these results in Fig. 6, which the stretching deformation of four corners is uniform due the effect of the I-SPH method combined with the AV. As a result, it is necessary to adopt the AV in the I-SPH method.

Example 3: Deformation of a single Oldroyd-B fluid droplet impacting on plate [3,26]

In order to further investigate the necessity of the DR technique including that the AV and AS have been simultaneously added into the proposed I-SPH method, a single Oldroyd-B fluid droplet impact problem (see [3,26]) is studied by the I-SPH method combined with other techniques (see Figs. 7, 8). The initial parameters of drop are chosen as: Its initial diameter and velocity are $D = 0.02$ m and $U_0 = -1$ m s^{-1}, respectively. The total viscosity is $\eta = 4$ Pa $\cdot$ s, the ratio of Newtonian viscosity and total viscosity is $\beta_0 = 0.5$, the reference density is $\rho_0 = 10^3$ kg m^{-3}, the speed of sound is $c = 12$ m s^{-1}, the gravitational force acts downwards with $g_y = -9.81$ m s^{-2}, $\lambda_{0b} = 0.02$ s. For the simulations, the number of fluid particles is set to 1,981, the smoothing length $h = 1.4d_0$. The time-step is 1×10^{-5}s; The AV parameters

$\alpha_\Pi = 1$ and $\beta_\Pi = 1$ for all cases in this work. To remove the tensile instability, the AS coefficient $b = 0.5$. The dimensionless parameters Reynolds number and Weissenberg number are introduced as $Re = \rho DU_0/\eta$, $We = \lambda_{0b}U_0/D$, and corresponding to $Re = 5$, $We = 1$ in Figs. 7 and 8.

Figure 7 shows the particles distributions of an Oldroyd-B drop impacting on plate obtained by different methods at dimensionless time $t \approx 2.1$. It can be seen that the droplet fractures unrealistically for the problem of Oldroyd-B droplet impacting without the AS term (see Fig. 7a, b), and the simulations may be eventually diverge. The tensile instability can be well eliminated by the AS in Fig. 7c, d, which indicates that the necessity of AS added into the I-SPH or I-SPH-AV method for simulating the problem of droplet impact. The pressure distribution of an Oldroyd-B drop impacting on plate is illustrated in Fig. 8 at dimensionless time $t \approx 1.8$. The phenomenon of pressure oscillations for the I-SPH method combined with other techniques is weakened, due to the effect of density re-nationalization.

Observing Figs. 5, 6, 7, and 8, we can get that: (1) the problem of pressure oscillations can be effectively reduced by the density re-nationalization technique, and the numerical accuracy is improved; (2) the particle distributions with AV are more uniform than those without it, the numerical accuracy and stability are improved, and the phenomenon of unphysical clustering is weakened; (3) the tensile instability can be eliminated by the AS. In a word, the three techniques mentioned are valid and necessary in the simulation of TSPH

Table 1 Comparisons of consumed CPU time using different methods for simulating Oldroyd-B droplet problem (corresponds to the case of Fig. 7)

Dimensionless time of drop falling	TSPH CPU time (s)	I-SPH CPU time (s)	I-SPH-AV-AS CPU time (s)	I-SPH-AV-AS-DR CPU time (s)
1.5	1215.32	1958.66	1985.66	1986.73
2.5	2161.98	3412.77	3507.43	3509.12
3.5	3038.72	4745.35	5025.35	5026.81
4.5	4016.55	6083.19	7762.17	7763.63

or I-SPH for the free surface flows. It is worth noting that the parameters of artificial viscosity and AS should be appropriately chosen for simulating different fluid flow problems.

Moreover, the numerical results mentioned above also show that the proposed boundary treatment is feasible and valid. The artificial viscosity coefficients $\alpha_\Pi = 1$ and $\beta_\Pi = 1$ and the AS coefficient $b = 0.25$ (for the Newtonian droplet), $b = 0.7$ (for the viscoelastic droplet) are chosen in the following numerical simulations.

An improved numerical method has its advantages and disadvantages. The merits of proposed I-SPH method over than the TSPH method have been demonstrated in the section, and the disadvantage of proposed method is that it owns greater computational cost than the TSPH method due to the obtained local matrix in I-SPH method. Table 1 shows that the consumed CPU time of the I-SPH method combined with other techniques and the TSPH method by simulating a single Oldroyd-B droplet impact problem (2,821 fluid particles, 903 virtual particles and the other simulation parameters correspond to the case of Fig. 7) in our computer. It can be observed that the CPU time of the proposed I-SPH method or I-SPH-AV-AS method is around 1.6 times than that of the Traditional SPH method. We can also know that the techniques of AS, artificial viscosity and DR technique occupy small computational cost from Table 1. As is well-known that the neighbor particle search technique has important influence on the CPU time of SPH or I-SPH method (see [12,45]), and a dynamic cells neighbor particle search method (see [12]) is adopted to enhance the computational effcency in the proposed particle method.

## 5 Numerical investigation of two viscoelastic droplets impacting on plate

According to References [1–4], the problem of droplet impacting on plate is an interesting and challenging case, which is often used to test the validity and capacity of proposed numerical method for simulating free surface. Only a single droplet falling on a rigid plate is considered in [3,4,42], and two droplets successively impacting problem is more complex than one droplet case (see [51]). Here, the deformation process of two intermiscible viscoelastic droplets falling
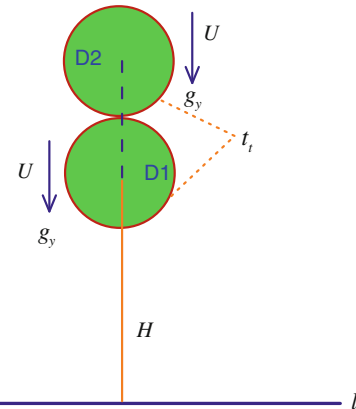
Fig. 9 The initial sketch of two droplets impacting on a plate

on a rigid plate in sequence is numerically predicted using the presented particle method for the purpose of demonstrating the capacity of proposed I-SPH combined with other techniques and displaying the complex non-linear viscoelastic behavior of polymer melts. Moreover, we know that the XPP model is affected by the stress singularity lower than some other rheological models based on phenomenological theory at higher Weissenberg number, and the XPP model can provide a good fitting to the rheological behaviors of branched polymer melts. According to Reference [42]. Thus the XPP model with some varied rheological parameters is mainly considered, and the Newtonian and Oldroyd-B model fluid are also presented for comparison.

The initial sketch of two droplets impacting on a plate in sequence is shown in Fig. 9. The initial parameters are set as: the droplet diameter $D = 0.02$ m; the height of the first falling droplet i.e. "D1" to the plate is $H = 0.04$ m, and the height of the second droplet i.e. "D2" to the plate is $H+D$ (the droplets D1 and D2 have same diameter); the reference density ρ_0, gravitational force g_y, falling velocity U, speed of sound c and the smoothing length h are all the same as those in Fig. 7; the number of fluid particles for each droplet is 5025 and the time step $dt = 5 \times 10^{-6}$ s; the dimensionless time $t = t'U/D$ (t' is the real time) is adopted in this section. It is worth noting that the falling time interval of two droplets is denoted as "t_t" as shown in Fig. 9. Three phases of spreading process usually appear after a viscoelastic droplet impacting
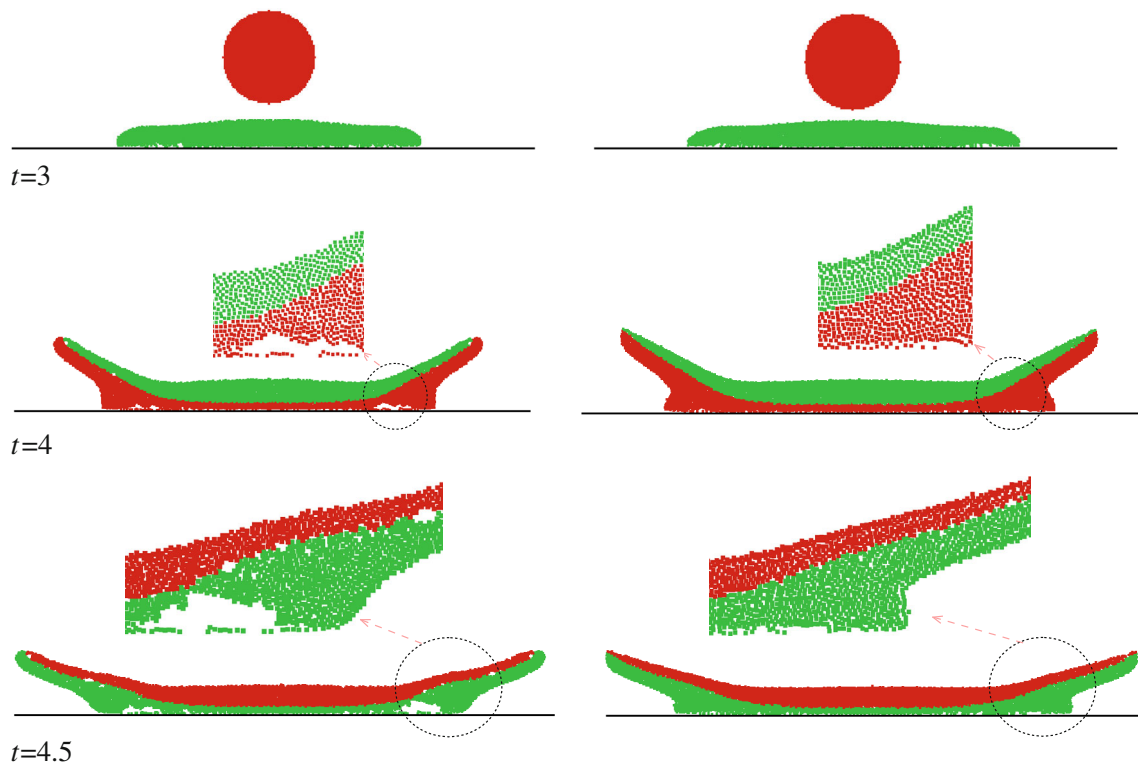
Fig. 10 The shape of two Oldoryd-B fluid droplets impacting on plate at different dimensionless time obtained by different methods with $Re = 60$, $We = 1$, $t_t = 3$: KGC-SPH method (*first column*), proposed I-SPH method (*second column*)

(see [1,3]), in which the second phase is the "contract stage". In the following simulations, three different typical $t_t = 0$, t_s, t_c are considered, which represent the two droplets falling at the same time ($t_t = 0$), the droplet D2 falling at the start time ($t_t = t_s$) of "contract stage" and the droplet D2 falling at the end time ($t_t = t_c$) of "contract stage", respectively. Only the droplet D1 falls on the plate when $t_t \to \infty$.

In order to demonstrate the main merit of proposed I-SPH method over than the KGC-SPH method (see Eqs. (28)–(32 in Sect. 3.2) or in [40]) for simulating the viscoelastic free surface, the shapes of two Oldoryd-B fluid droplets impacting on plate at different dimensionless time obtained by different methods with $Re = 60$, $We = 1$, $t_t = 3$ (the other parameters are the same as in Fig. 8) are shown in Fig. 10 (the red color and green color represent the droplet D2 and droplet D1 in Fig. 10, respectively.). In a short time after the droplet D1 impacts on the plate, the numerical results obtained by the I-SPH and KGC-SPH is similar and acceptable. The undesired results of using the KGC-SPH appears versus time after the droplet D2 falling on the droplet D1 ($t = 4$ or $t = 4.5$), especially near the rigid wall and on the intersection area of two droplets. However, the I-SPH results are still acceptable. The main reason is that the obtained local matrix in KGC-SPH method has worse non-sigularity than that in the I-SPH method, especially near the boundary of simulating region. Meanwhile, the simulation of using KGC-SPH may be ter-
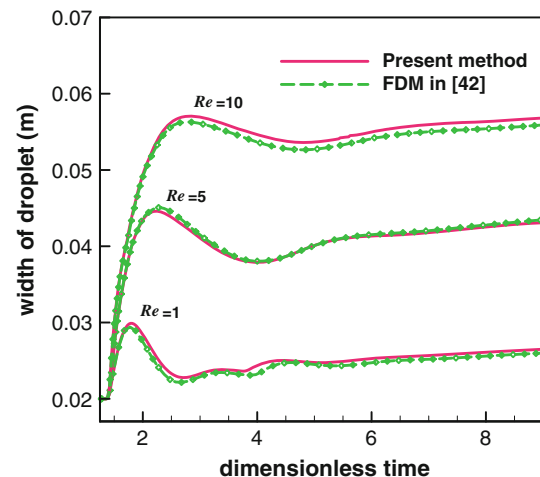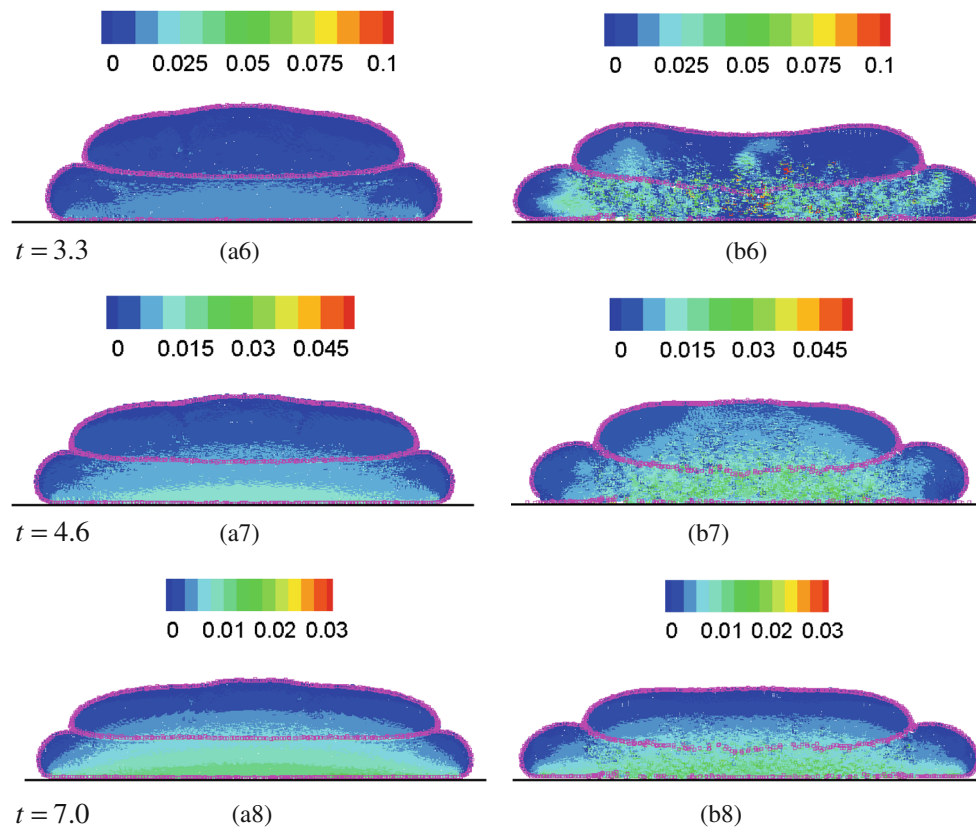

Fig. 11 The width of single XPP droplet after impacting on plate versus dimensionless time with $We = 1$

minated at sometime due to the serious singularity of local matrix near the boundary of simulating area. Moreover, the computational cost of the proposed I-SPH method is lower than that of the KGC-SPH method in these simulations, for example the consumed CPU time of using the KGC-SPH is 1,353.6 s and the consumed CPU time of using the I-SPH is 1,285.3 s under the same computational condition when the simulation step equals to 10,000.

Fig. 12 The spreading process and pressure distributions ($p/(\rho g)$) of two droplets impacting on plate with $Re = 5$, $We = 1$, $t_t = 0$: the *first column* is Newtonian fluid (**a1**–**a8**); the *second column* is Oldroyd-B fluid (**b1**–**b8**)

$t = 3.3$ (a6)   (b6)

$t = 4.6$ (a7)   (b7)

$t = 7.0$ (a8)   (b8)
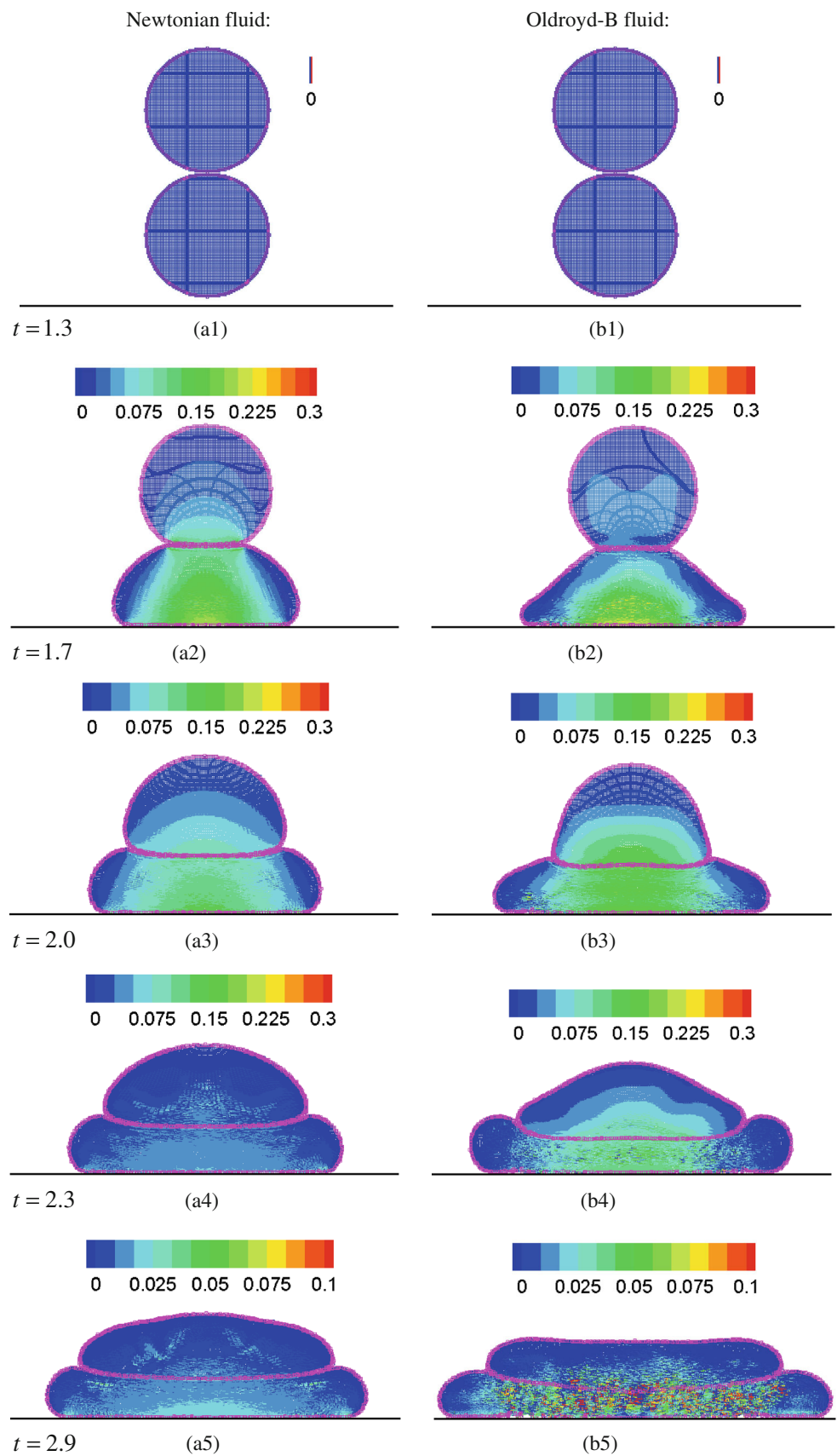
Fig. 12 continued

To further illustrate the reliability of using proposed method to simulate the deformation process of droplet impacting on plate based on the XPP model, the width of a single XPP droplet D1 after impacting is shown in Fig. 11 and compared with the FDM results (see [42]). In Fig. 11, the model parameters $\alpha_0 = 0.01, q = 4, \beta_0 = 0.1, er = 0.8$, and the $\lambda_{0b} = 0.02$ s corresponding to Weissenberg number $We = \lambda_{0b}U/D = 1$, the total viscosity $\eta = 20, 4, 2$ Pa·s corresponding to Reynolds number $Re = \rho_0 DU/\eta = 1, 5, 10$, respectively.

Figure 11 shows the numerical results with different Reynolds number $1 \leq Re \leq 10$, and the results obtained by the I-SPH method are in good agreement with the FDM results. It can be seen that the width of droplet increases significantly as Re increases after impacting. As a consequence, the viscous force relative to inertial force decreases when the droplet reaches the plate, which leads to an increased width.

5.1 Influence of falling time interval on the deformation process

The deformation process of viscoelastic droplet becomes more complex while another intermiscible droplet falls on the former droplet. The falling time interval has an important influence on the spreading process of droplet D1, which

can be seen from Figs. 12, 13, 14, and 15. The "pink" color near boundary of droplets in Figs. 12 and 15 represents the sketch of deformation process of two droplets.

Figure 12 shows the spreading process and pressure distributions $(p/(\rho g))$ of two droplets impacting on plate with $Re = 5, We = 1, t_t = 0$, and the other parameters are the same as those in Fig. 11. It can be seen the variations of deformation process and pressure field of droplets D1 and D2 from Fig. 12. The width of droplets D1 and D2 versus time obtained by different methods for the Newtonian and Odroyd-B fluid are shown in Fig. 13, respectively. From Fig. 13, the results of two Oldroyd-B droplets successively impacting problem obtained using the present method are close those obtained using the FVM method combined with Level-Set technique (see [9]), and show that the proposed particle method is credible for simulating two viscoelastic droplets impact problem. Observing Figs. 12 and 13, we can also know that: (1) The pressure is significantly increased at the moment after impacting, and it is slowly decreased with the increased impacting time (see Fig. 12). (2) The deformation process for the Oldryod-B droplet has three stage because the influence of elastic stress and the deformation for the Newtonian droplet keeps spreading on the plate, but the shape is different from the case of a single droplet impacting on plate (see [1,3,26]) at the same time. Moreover, the
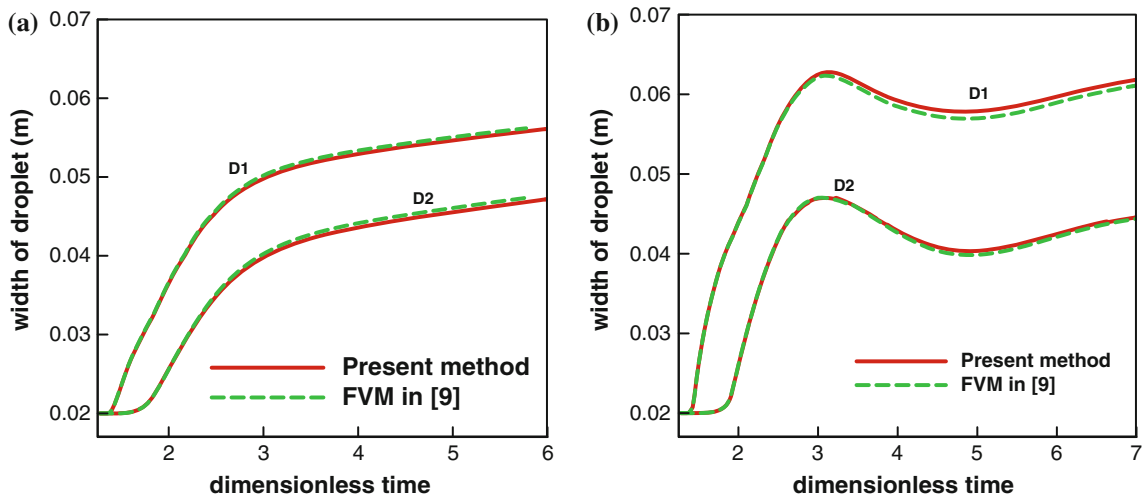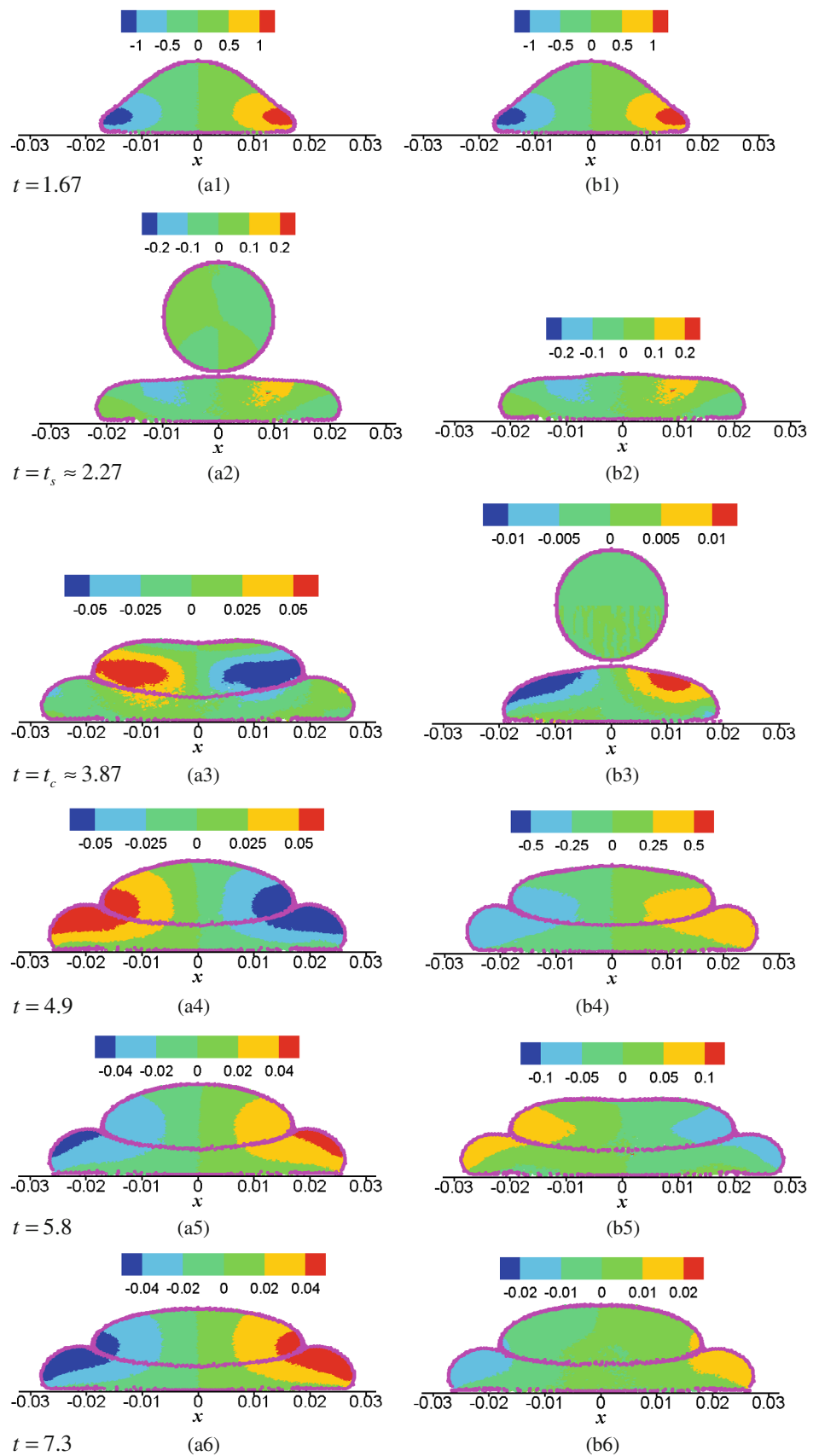
Fig. 13 The variation of the width of two droplets obtained using different methods for different model fluid after impacting on plate versus dimensionless time corresponds to the case of Fig. 12: **a** Newtonian fluid; **b** Oldroyd-B fluid ($t_t = 0$)
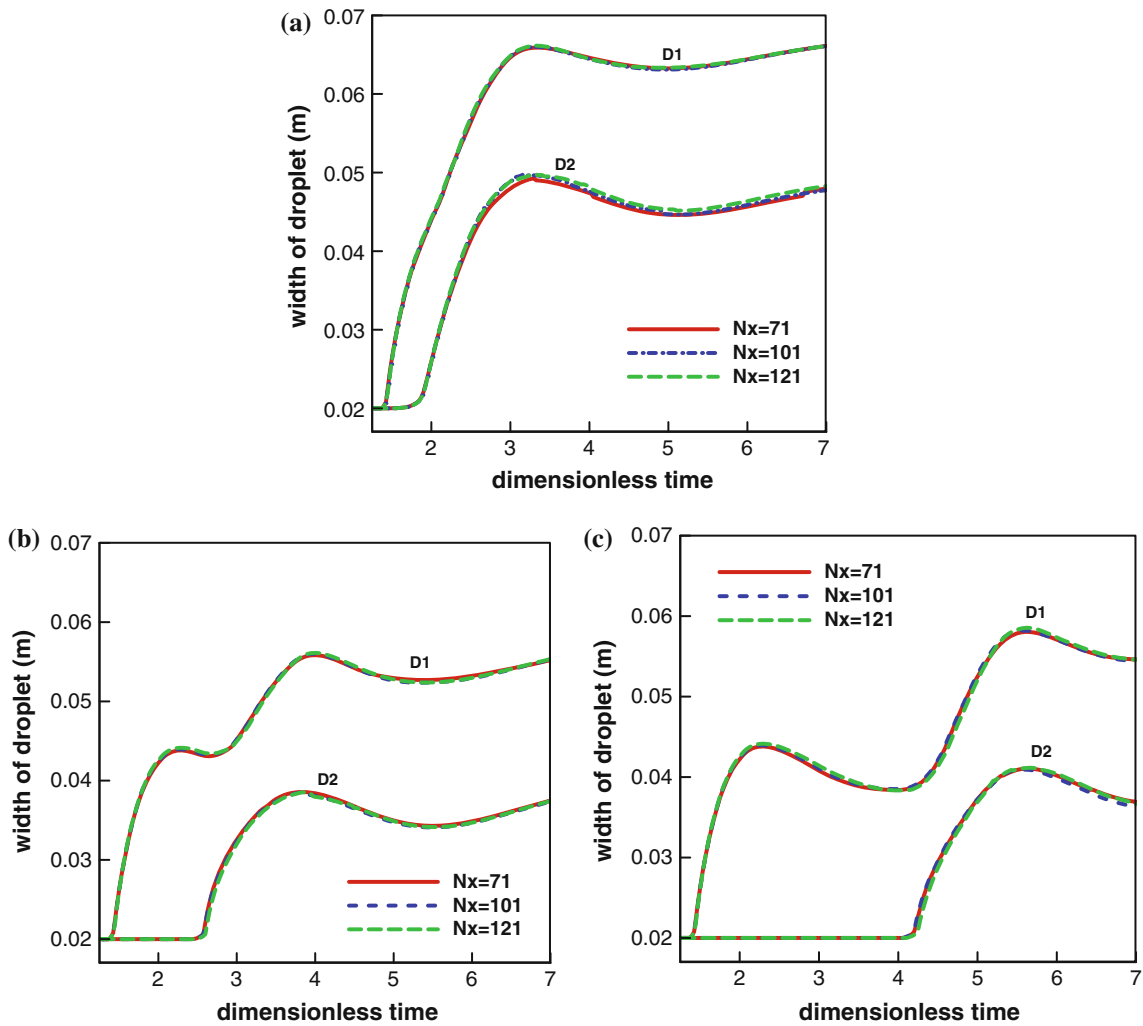
Fig. 14 The results of the width of two XPP droplets falling with different particle number at different time intervals ($We = 1$, $Re = 5$): **a** $t_t = 0$; **b** $t_t = t_s$; **c** $t_t = t_c$

Fig. 15 The deformation
process and v_x-velocity field of
two XPP droplets after falling
with $Re = 5$, $We = 1$ at the
time intervals corresponds to the
case of Fig. 14b, c: (**a1**–**a6**)
$t_t = t_s$ (*first column*); (**b1**–**b6**)
$t_t = t_c$ (*second column*)

$t = 1.67$ (a1)

(b1)

$t = t_s \approx 2.27$ (a2)

(b2)

$t = t_c \approx 3.87$ (a3)

(b3)

$t = 4.9$ (a4)

(b4)

$t = 5.8$ (a5)

(b5)

$t = 7.3$ (a6)

(b6)

spreading tendency of the droplets D1 and D2 for the Newtonian fluid or Oldroyd-B fluid along the plate is weaker than that of a single droplet impacting on plate due to the interaction between two droplets. (3) The deformation tendency of droplet D1 is more violent than that of the droplet D2 because the effect of extrusion between the droplet D2 and rigid plate, while the changing curve of width of droplet D1 is parallel with the case of droplet D2 for the Newtonian fluid or Odroyd-B fluid (see Fig. 13). (4) The phenomenon of cave for the droplet D2 based on the Oldroyd-B model is obviously observed from Fig. 12b6. (5) For the reason of the interaction between droplets, the phenomenon of deformation for the droplet D1 is more complex than that for a single droplet impacting on plate (see [1,3,26]). The remarks mentioned above are similar to the experimental conclusions of two water droplets successive falling on a solid in [51].

In order to investigate the influence of falling time interval on the deformation process, the width of two XPP droplets D1 and D2 after falling with $Re = 5$, $We = 1$ at three typical time intervals is shown in Fig. 14. Meanwhile, the better numerical convergence of the present improved particle method for simulating two XPP droplets impact problem is discussed in Fig. 14 ("Nx" denotes the fluid particles number along the x-axis at initial particles distribution), and the reliability of the proposed method is also checked. The model parameters are all the same as those in Fig. 11 except for the falling time interval t_t. The spreading tendency along the plate for two XPP droplets D1 and D2 is weaker than that for two Oldroyd-B droplets by comparing Figs. 13b and 14a. The reason is the influence of branched polymer melts rheological parameters. The spreading process of droplet D1 with $t_t = t_s$ and $t_t = t_c$ (see Fig. 14b, c) is more complex than that of droplet D1 with $t_t = 0$ (see Fig. 14a). Particularly, the contract deformation process of droplet D1 occurs twice at $t_t = t_c$ while the contract tendency occurs only once in the case of a single droplet impacting at $Re = 5$ which can be observed from Figs. 14c and 11, respectively. The effect of elastic stress is illustrated once again after the droplet D2 impacting on the droplet D1 in Fig. 14b, c, and consequently a faster spreading of droplet D1 appears in a short time after the droplet D2 falls on the D1.

The part of potential energy of droplet D2 is transformed into the energy of motion of droplet D1, but the total mechanical energy rapidly reduces after impacting, which can be observed from Fig. 15. Figure 15 shows that the spreading process and v_x-field of two droplets D1 and D2 after impacting at time intervals $t_t = t_s$ and $t_t = t_c$, which corresponds to the case of Fig. 14b, c, respectively. According to the variation of velocity field, the deformation tendency at different dimensionless time can be easily understood, and the contract deformation phenomenon corresponds to the positive values of velocity field along the negative direction of x-axis (see Fig. 15a4, b5). The v_x-field near the two ends of
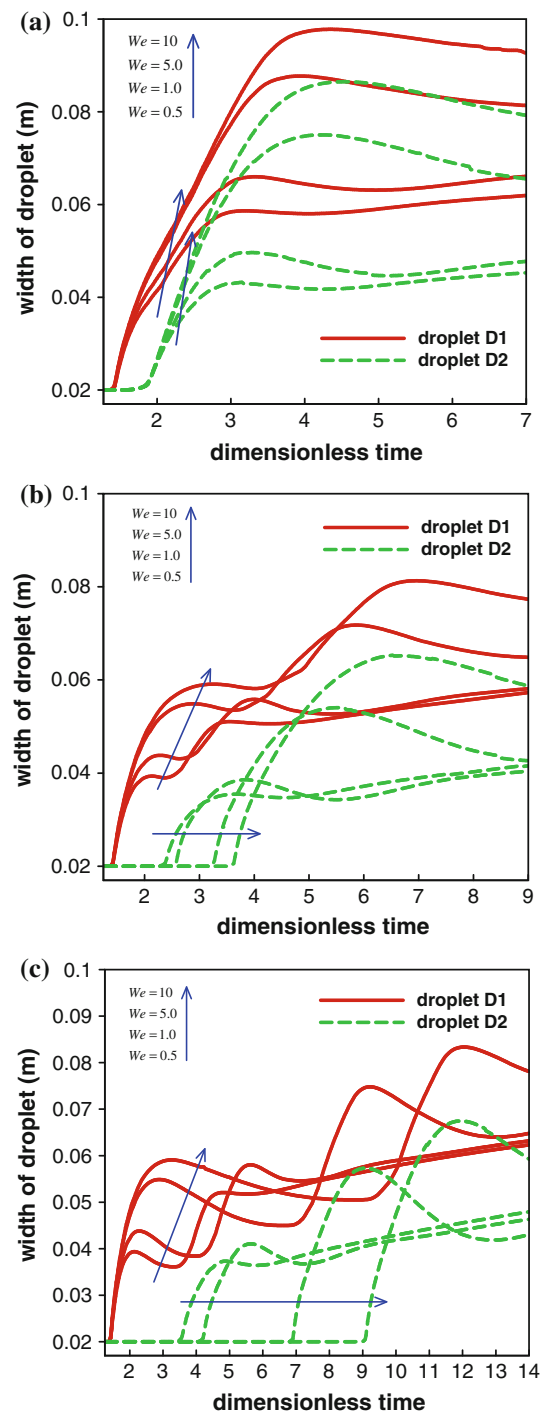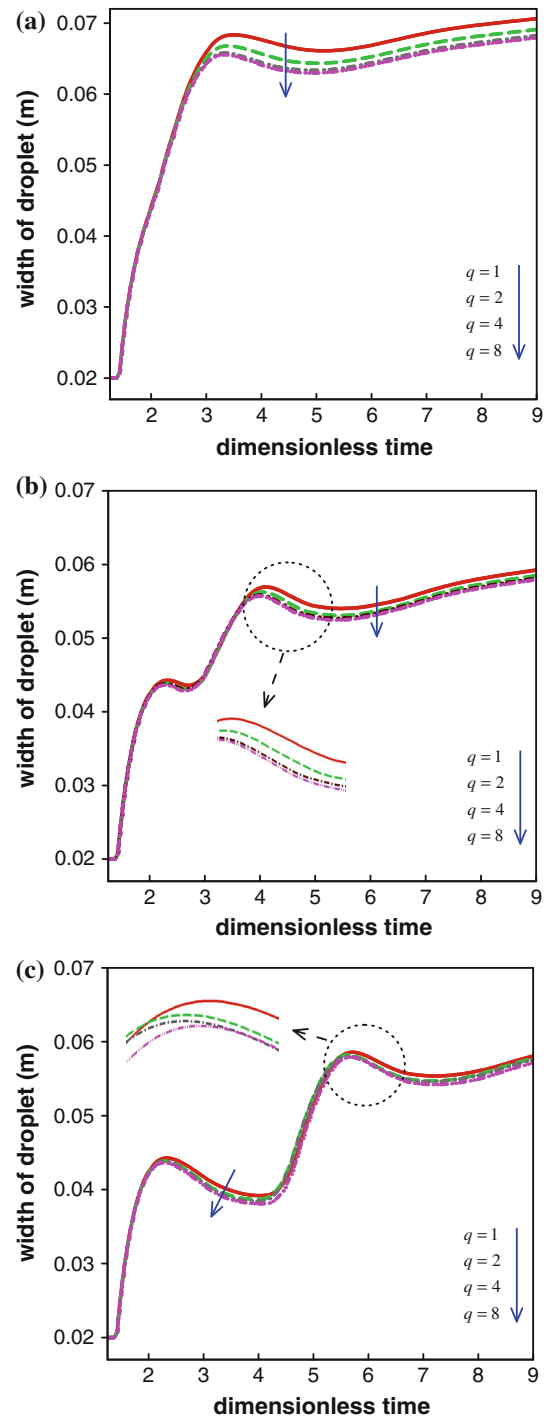

Fig. 16 The variation of the width of two XPP droplets versus dimensionless time with the influence of We at different time intervals: **a** $t_t = 0$; **b** $t_t = t_s$; **c** $t_t = t_c$

droplet D1 is increased in a short time when only the droplet D1 impacts the plate, and decreased with the increased impacting time. Subsequently, the velocity values are also increased in a short time after droplet D2 impacts on D1, and decreased versus impacting time which can be observed from Fig. 15b3–b6.

(a)

(b)

(c)
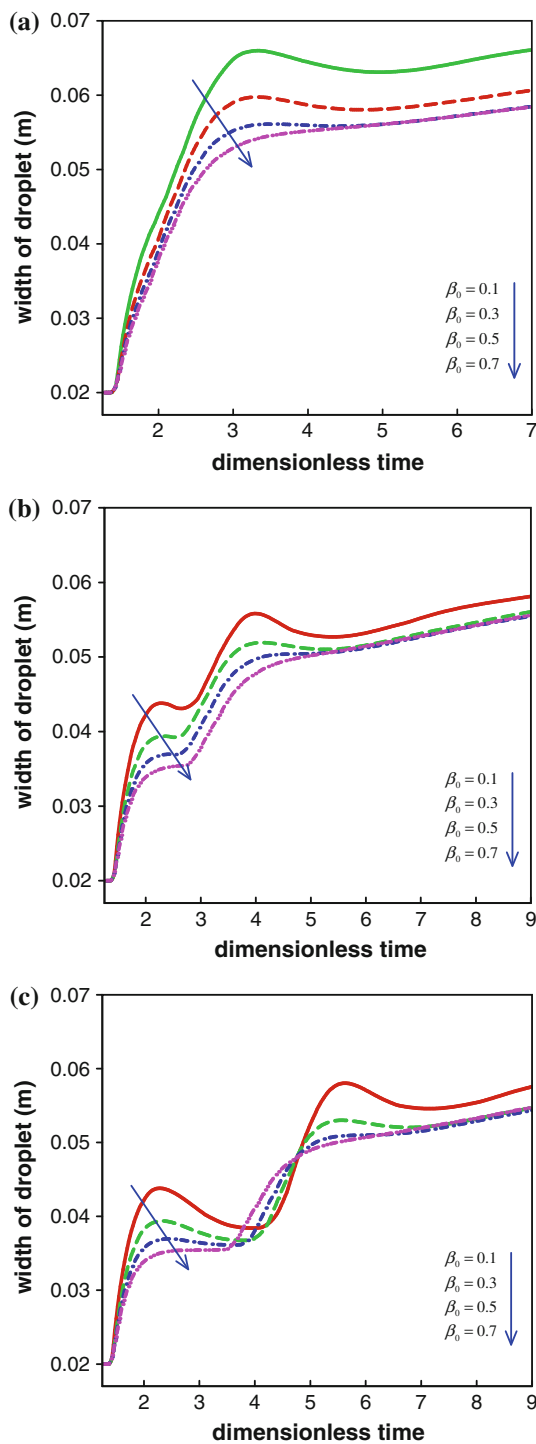
Fig. 17 The variation of the width of the XPP droplet D1 versus dimensionless time with the influence of β_0 at different time intervals: **a** $t_t = 0$; **b** $t_t = t_s$; **c** $t_t = t_c$

(a)

(b)

(c)

Fig. 18 The variation of the width of the XPP droplet D1 versus dimensionless time with the influence of q at different time intervals: **a** $t_t = 0$; **b** $t_t = t_s$; **c** $t_t = t_c$
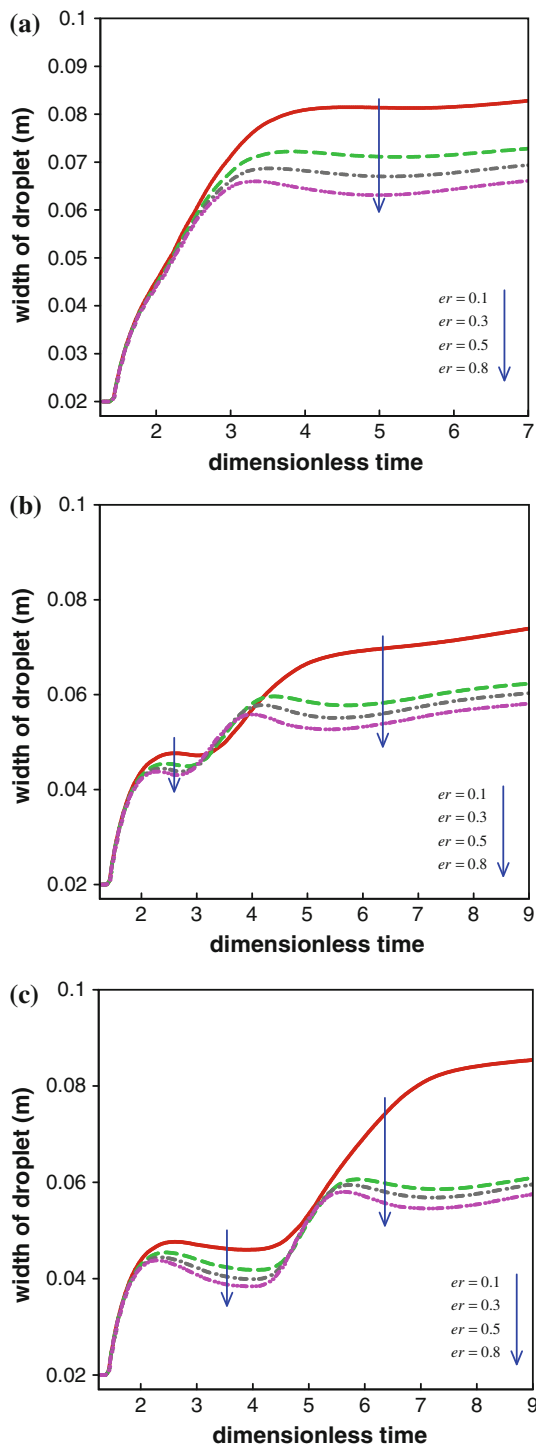
In a word, the falling time interval has an important influence on the deformation process of two droplets especially for the droplet D1, which makes the spreading process of two droplets impacting on plate more complex than that of a single droplet impacting problem.

5.2 Influence of model parameters on the deformation process

To further demonstrate the important influence of model parameters on the spreading process of droplets D1 and D2 impacting on plate and the capacity of the proposed method to

(a)

(b)

(c)

Fig. 19 The variation of the width of the XPP droplet D1 versus dimensionless time with the influence of *er* at different time intervals: **a** $t_t = 0$; **b** $t_t = t_s$; **c** $t_t = t_c$

parameters of β_0, *er*, and *q* are also shown in Figs. 17, 18 and 19, respectively.

With the Weissenberg number increases, the larger value of width of droplets D1 and D2 is gained at different time (see Fig. 16). The start retraction time of spreading process of XPP droplets D1 and D2 is delayed, and the relative retraction phase is elongated (see Fig. 16b, c), which is a consequence of the elongation of stretch relaxation time λ_{0b} as We increases. The spreading tendency of droplet D2 is still similar to the case of droplet D1 with different We at different time intervals after the droplet D2 impacts on the D1. Then, only the variation curve of spreading process of the droplet D1 is shown at different time intervals in Figs. 17, 18 and 19.

The influence of solvent contribution on two droplets impact problem is displayed in Fig. 17. The behavior of XPP fluid is more close to the Newtonian fluid behavior as β_0 increases, which represents the reduction of effect of elastic stress. The change of width with different β_0 in a short time after impacting is obvious, and the spreading process of droplet is slower when β_0 increases. Moreover, we also can observe that the spreading process of XPP droplet becomes slow as both *q* and *er* increase (see Figs. 18, 19). However, the change of width of droplet for different Pom–Pom molecule parameter *q* is small in the impacting process which implies that the influence of *q* is relatively small. All the results in Figs. 16, 17, 18, and 19 indicate that the macroscopic model parameters We, β_0 and *er* have more important influence on the spreading process of two droplets impact problem than the parameter *q*, which is in agreement with the related conclusions given in [42].

6 Conclusions

In this work, the spreading process of two XPP droplets falling on a plate in sequence with different time intervals is numerically predicted by using an improved SPH (I-SPH) method combined with other treat techniques. The proposed I-SPH method is motivated by a coupled concept in which the traditional SPH (TSPH) method is used near the boundary area and a KGC-SPH method is used in the interior fluid field. The KGC-SPH method is achieved by correcting the first order kernel gradient of TSPH without kernel derivative. Meanwhile, an AS technique is presented to eliminate the tensile instability, a periodic DR technique is considered for restraining the oscillation of pressure, and a new boundary condition treatment is used to prevent fluid particles from penetrating the rigid plate.

The ability and merits of proposed I-SPH method are tested by simulating two benchmark problems and a single droplet impact problem. The problem of two XPP droplets impacting on plate is numerically investigated using the I-SPH method and the influences of falling time interval and

simulate two XPP droplets impact problem, Fig. 16 shows the width of the XPP droplets D1 and D2 with increasing Weissenberg number at three typical falling time intervals. The widths of the XPP droplet D1 with three increasing model

model parameters on the deformation process of droplets impacting on plate are also analyzed. All the results show that: (1) the proposed I-SPH method possesses higher accuracy and better stability than TSPH method; (2) it is valid and necessary to introduce the AS and DR techniques into the I-SPH method to simulate the droplet impacting problem; (3) the proposed boundary condition treatment is feasible; (4) the spreading process of two viscoelastic droplets impact is more complex than that of a single droplet impact problem; (5) the contract stage of XPP droplets after impacting may be occur twice as the model parameters and falling time interval are appropriately chosen; (6) the macroscopic model parameters have significant influences on the deformation process of two viscoelastic droplets impact problem.

References

1. Tomé MF, Castelo A, Ferreira VG, McKee S, Walters K (2007) Die-swell, splashing drop and a numerical technique for solving the Oldroyd-B model for axisymmetric surface flows. J Non-Newtonian Flu Mech 141:148–166
2. Lunkad Siddhartha F, Buwa Vivek V, Nigam KDP (2007) Numerical simulations of drop impact and spreading on horizontal and inclined surfaces. Chem Eng Sci 62:7214–7224
3. Tomé MF, Mangiavacchi N, Castelo A, Cuminato JA, McKee S (2002) A finite difference technique for simulating unsteady viscoelastic free surface flows. J Non-Newtonian Fluid Mech 106:61–106
4. Jiang T, Ouyang J, Yang B, Ren J (2010) The SPH method for simulating a viscoelastic drop impact and spreading on an inclined plate. Comput Mech 45:573–583
5. Vebeeten WMH, Peters GWM, Baaijens FPT (2001) Differential constitutive equations for polymer melts: The extended Pom-Pom model. J Rheol 45:823–843
6. McKee S, Tomé MF, Ferreira VG, Cuminato JA, Castelo A, Sousa FS, Mangiavacchi N (2008) The MAC method. Comput Fluids 37:907–930
7. Hirt CW, Nicholls BD (1981) Volume of fluid (VOF) method for dynamics of free boundaries. J Comput Phys 39:201–221
8. Osher S, Sethian JA (1988) Fronts propagating with curvature-dependent speed: algorithms based on Hamilton-Jacobi formulations. J Comput Phys 79:12–49
9. Li Q, Ouyang J, Yang B, Jiang T (2011) Modelling and simulation of moving interfaces in gas-assisted injection moulding process. Appl Math Model 35:257–275
10. Li S, Qian D, Liu WK, Belytschko T (2000) A mesh-free contact-detection algorithm. Comput Methods Appl Mech Eng 190:3271–3292
11. Li S, Liu WK (2002) Mesh-free particle methods and their applications. Appl Mech Rev 54:1–34
12. Liu GR, Liu MB (2003) Smoothed particle hydrodynamics: a mesh-free particle method. World Scientific, Singapore
13. Liu MB, Liu GR (2010) Smoothed particle hydrodynamics (SPH): an overview and recent developments. Arch Comput Methods Eng 17:25–76
14. Monaghan JJ (1994) Simulating free surface flows with SPH. J Comput Phys 110:399–406
15. Flebbe O, Munzel S, Herold H et al (1994) Smoothed particle hydrodynamics-physical viscosity and the simulation of accretion disks. Astrophys J 431:754–760
16. Morris JP, Fox PJ, Zhu Y (1997) Modeling low Reynolds number incompressible flows using SPH. J Comput Phys 136:214–226
17. Cleary PW, Monaghan JJ (1999) Conduction modeling using smoothed particle hydrodynamics. J Comput Phys 148:227–264
18. Cummins SJ, Rudman M (1999) An SPH projection method. J Comput Phys 152:584–607
19. Shao S, Lo EYM (2003) Incompressible SPH method for simulating Newtonian and non-Newtonian flows with a free surface. Adv Water Resour 26(7):787–800
20. Monaghan JJ, Kocharyan A (1995) SPH simulation of multi-phase flow. Comput Phys Commun 87:225–235
21. Colagrossi A, Landrini M (2003) Numerical simulation of interfacial flows by smoothed particle hydrodynamics. J Comput Phys 191:448–475
22. Hu X, Adams N (2006) A multi-phase SPH method for macroscopic and mesoscopic flows. J Comput Phys 213:844–861
23. Monaghan JJ (2002) SPH compressible turbulence. Mon Not R Astron Soc 335:843–852
24. Ellero M, Kröger M, Hess S (2002) Viscoelastic flows studied by smoothed particle dynamics. J Non-Newtonian Fluid Mech 105:35–51
25. Ellero M, Tanner RI (2005) SPH simulations of transient viscoelastic flows at low Reynolds number. J Non-Newtonian Fluid Mech 132:61–72
26. Fang J, Owens RG, Tacher L, Parriaux A (2006) A numerical study of the SPH method for simulating transient viscoelastic free surface flows. J Non-Newtonian Fluid Mech 13:68–84
27. Liu WK, Jun S, Zhang YF (1995) Reproducing kernel particle methods. Int J Numer Methods Fluids 20:1081–1106
28. Li SF, Liu WK (1999) Reproducing kernel hierarchical partition of unity. part I-formulation and theory. Int J Numer Methods Eng 45:251–288
29. Li SF, Liu WK (1999) Reproducing kernel hierarchical partition of unity, part II-applications. Int J Numer Methods Eng 45:251–288
30. Chen JK, Beraun JE (2000) A generalized smoothed particle hydrodynamics method for nonlinear dynamic problems. Comput Methods Appl Mech Eng 190:225–239
31. Liu MB, Liu GR (2006) Restoring particle consistency in smoothed particle hydrodynamics. Appl Numer Math 56:19–36
32. Zhang GM, Batra RC (2004) Modified smoothed particle hydrodynamics method and its application to transient problems. Comput Mech 34:137–146
33. Batra RC, Zhang GM (2007) Search algorithm and simulation of elastodynamic crack propagation by modified smoothed particle hydrodynamics (MSPH) method. Comput Mech 40:531–546
34. Zhang GM, Batra RC (2009) Symmetric smoothed particle hydrodynamics (SSPH) method and its application to elastic problems. Comput Mech 43:321–340
35. Batra RC, Zhang GM (2008) SSPH basis functions for meshless methods, and comparison of solution of solutions with strong and weak formulations. Comput Mech 41:527–545
36. Liu MB, Xie WP, Liu GR (2005) Modeling incompressible flows using a finite particle method. Appl Math Model 29:1252–1270
37. Tao Jiang, Jie Ouyang, Jinlian Ren (2012) A mixed corrected symmetric SPH (MC-SSPH) method for computational dynamic problems. Comput Phys Commun 183:50–62
38. Oger G, Doring M, Alessandrini B, Ferrant P (2007) An improved SPH method: towards higher order convergence. J Comput Phys 225:1472–1492

39. Fetehi R, Manzari MT (2012) A consistent and fast weakly compressible smoothed particle hydrodynamics with a new wall boundary condition. Int J Num Methods Fluids 68:905–921

40. Ren JL, Ouyang J, Jiang T, Li Q (2011) Simulation of complex filling process based on the generalized Newtonian model using a corrected SPH scheme. Comput Mech 49:643–665

41. Wang W, Li XK, Han XH (2009) Equal low-order finite element simulation of the planar contraction flow for branched polymer melts. Polym Plast Technol Eng 48:1158–1170

42. Oishi CM, Martins FP, Tomé MF, Alves MA (2012) Numerical simulation of drop impact and jet buckling problems using the eXtended Pom-Pom model. J Non-Newtonian Fluid Mech 169–170:91–103

43. Wendland H (1995) Piecewise polynomial, positive definite and compactly supported radial functions of minimal degree. Adv Comput Math 4:389–396

44. Fang J, Parriaux A, Rentschler M, Ancey C (2009) Improved SPH methods for simulating free surface flows of viscous fluids. Appl Numer Math 59:251–271

45. Monaghan JJ (2005) Smoothed particle hydrodynamics. Rep Prog Phys 68:1703–1759

46. Swegle JW, Hicks DL, Attaway SW (1995) Smoothed particle hydrodynamics stability analysis. J Comput Phys 116:123–134

47. Monaghan JJ (2000) SPH without a tensile instability. J Comput Phys 159:290–311

48. Gray JP, Monaghan JJ, Swift RP (2001) SPH elastic dynamics. Comput Methods Appl Mech Eng 190:6641–6662

49. Yildiz M, Rook RA, Suleman A (2009) SPH with the multiple boundary tangent method. Int J Numer Methods Eng 77:1416–1438

50. Xu R, Stansby P, Laurence D (2009) Accuracy and stability incompressible SPH (ISPH) based on the projection method and a new approach. J Comput Phys 228:6703–6725

51. Fujimoto H, Ito S, Takezaki I (2002) Experimental study of successive collision of two water droplets with a solid. Exp Fluids 33:500–502